Revision 2

Title

Experimental constraints on bubble formation and growth during magma ascent: A Review

Authors and affiliations

Adrian Fiege[1] and Sarah B. Cichy [2] *

[1] Department of Earth and Environmental Sciences, University of Michigan, 1100 North University Ave, Ann Arbor, MI 48109-1005, USA

[2] School of Earth & Space Exploration, Arizona State University, 781 E. Terrace Mall, Tempe, AZ 85287-6004, USA

e-mails: afiege@umich.edu; scichy@asu.edu

*corresponding author *Fax:* +1 480-965-8102; *Phone:* +1 480-727-2557

Abstract

The number of studies investigating the vesiculation of natural samples and their implications to volcanic degassing and eruption mechanisms has been growing rapidly within the last decades. In order to interpret the natural rock textures, the geoscience community has produced a range of experimental and theoretical datasets on bubble nucleation, growth and coalescence in magmatic systems. A robust experimental database is required to calibrate (theoretical and empirical) modeling approaches, which allow the calculation of magma ascent rates from erupted volcanic ejecta mainly by the determination of the bubble number density (BND). Although, the available

dataset is still limited, it already shows that variations in melt (and volatile/fluid) composition can have a significant effect. In this manuscript we (re-)evaluate the existing experimental dataset, while focusing mainly on the review and discussion of continuous decompression experiments.

One aim of this review article is to encourage scientists to fill the gaps in the existing experimental datasets and help to acknowledge, use and further develop the most promising experimental techniques. Therefore, we highlight different methods and discuss their advantages and possible limitations. We also discuss possible ways of how to better account for the influence of melt composition in models, which link BND to decompression rate.

Keywords

bubble nucleation and growth, decompression experiment, magma ascent rates

1. Introduction and Motivation

Large amounts of H_2O, CO_2, SO_2 and Cl are released by volcanic systems. However, the estimated annual volcanic emission of the "greenhouse gas" CO_2 to the atmosphere is ~0.1 to 0.44 Gt and, thus, about a factor of 80 to 270 lower than the anthropogenic CO_2 in 2010 (Friedlingstein et al, 2010). On the other hand, the global anthropogenic SO_2 emission ranges around 100 to 110 Mt within the last decade (Klimont et al., 2013), while a single eruption of a major volcano, such as the Mt. St. Helens eruption in 1480, the Tambora eruption in 1815 or the eruption of Krakatau in 1885, can increase the annual SO_2 emission by up to 70% (see Shinohara, 2008; and references therein). Although the man-made greenhouse gas emission is without a doubt exceeding the volcanic contribution, large eruptions such as the one of Mt.

Pinatubo (Philippines) in 1991 can release tremendous amounts of CO_2 (here: ~42 Mt CO_2) and SO_2 (here: ~17-20 Mt SO_2) over a short period (e.g., Bluth et al., 1992; Gerlach et al., 1996) and, thus, impact the global climate for months and even up to several years (e.g., Self et al., 1996). Notably, SO_2 is a much more efficient climate affecting gas than CO_2. It is largely converted to sulfuric acid after being released to the atmosphere, where it condenses rapidly to form fine grained sulfate aerosols. The sulfate aerosol increases the reflection of radiation from the sun into space, causing the cooling of Earth's atmosphere and/or troposphere (McGee et al., 1997). Other possible major environmental impacts of S emission include: ozone depletion (via reaction with Cl; Self et al., 1996) and acid rain leading, amongst others, to significant crop failure (Sigurdsson, 1982). Although there is nothing (geo-)scientists can do about this natural contribution to climate change, the (physico-chemical) way on how the volatiles separate from a magma or lava is crucial for our understanding of eruption mechanisms and, thus, is helpful in forecasting volcanic eruptions and in possibly predicting the future impact of volcanic activities on the global climate.

Magma degassing, for instance during magma ascent (i.e., decompression-induced) or magma cooling (e.g., crystallization-induced second boiling), leads to the formation of bubbles, which can grow and/or coalesce over time and even separate the gas phase completely from the residual melt or magma (e.g., Sparks et al., 1994). The vesiculation of a magma, and here especially the size and number of bubbles, changes magma viscosity and, thus, significantly affects the eruptive style, i.e., "harmless" effusive vs. potentially "hazardous" explosive. The vesiculation of (natural and experimental) samples is typically described by the bubble number density (BND) and is a characteristic feature of some volcanic products (e.g., pumice, tephra) that can help to elucidate

the "ascent-history" of an erupted magma (e.g., Sparks et al., 1994; Toramaru, 1995; 2006; Hamada et al., 2010).

Once bubble nucleation is triggered and a certain vesiculation in a magma is reached, the bubbles may start to connect and form a bubble network along which large amounts of fluid can be transported upwards (Edmonds et al., 2010). This process may be limited to regimes with significant shear strain within the magma, e.g., along the conduit or in magma chambers with strong convections (e.g., Namiki and Manga, 2008; Namiki, 2012). It is worth noting that in systems with radii of >5 mm for the largest bubbles, interaction between bubbles can induce significant bubble deformation (Manga and Stone, 1994), which may favor the formation of interconnected bubble networks. Even though an effective transport of fluids via bubble networks within a magma chamber may be questioned, the diffusive coarsening and bubble ascent from an underplating mafic magma to an overlaying felsic magma is probably an important process to transport volatiles and precious metals (e.g., Cu) from the mafic to the overlaying felsic magma and into fractures and intrusions where they can form porphyry-(Cu)-deposits (e.g., Hattori and Keith, 2001; Halter et al., 2005; Audétat and Simon, 2012). Although the majority of the fluids released by a magmatic system during an eruption may be transported to the surface along the conduit, these fluids may also play an important role in the formation of porphyry-(Cu)-deposits during periods of low volcanic activity (i.e., when bubbles have time to ascend). Thus, understanding bubble nucleation, growth and ascent in a magma at depth will also help elucidating timescales for the formation of porphyry deposits (and similar deposits).

In the last decades, several research groups worked on the experimental investigation of bubble nucleation processes in (silicate) melts. While the experimental and analytical techniques are continuously improving (see Section 2 and 3), we are getting more aware of the limitations of

certain techniques and a critical re-evaluation of the dataset is required. For instance, recently published experimental studies have revealed that the decompression style (continuous vs. stepwise) affects bubble formation to a significant extent (see Section 2 and Nowak et al., 2011; Marxer et al., 2015). This review focusses on decompression-induced bubble nucleation and aims at providing an overview of the existing experimental and analytical techniques as well as at the discussion and (re-)interpretation of previous results. Based on the compiled experimental literature data and three additional experiments performed for this study, we show that changes in major element composition and volatile contents can affect bubble nucleation considerably. However, the available dataset is still very limited and we highlight the existing gaps that should be filled in the near future, using the techniques described in this manuscript.

1.1 Theoretical background of bubble formation

When a volatile-supersaturated melt is cooled down or is depressurized, small clusters of gas molecules form and grow through volatile diffusion in the melt (e.g., Proussevitch et al., 1993; Proussevitch and Sahagian, 1996; 1998). Free energy and interfacial energy are linked to the formation of a separate gas phase and the creation of the bubble surface, respectively. The ratio between the two energies determines whether the critical (or minimum) bubble radius r_c ($r_c = 2 \cdot \sigma / \Delta P_N$) can be overcome, leading to either homogeneous or heterogeneous bubble nucleation; see, e.g., reviews by Sparks (1978) and by Sparks et al. (1994). In heterogeneous bubble nucleation, wetted crystal surfaces, e.g., of Fe-Ti-oxides (Hurwitz and Navon, 1994), can act as bubble nucleation sites, lowering the required supersaturation pressure (ΔP_N; difference between gas pressure in the melt and ambient pressure) and, thus, decreasing the critical bubble radius r_c (see Section 4.2). The melt-surface tension (σ) is a function of the hydrous melt composition and

115 increases with higher silica content (Mangan and Sisson, 2005), negatively influencing the
116 nucleation rate (J). The strong dependence of the surface tension on melt composition was
117 recently confirmed by experiments performed by Masotta et al. (2014) in an externally heated
118 diamond anvil cell, using basaltic, andesitic and rhyodacitic melts. In contrast, the study of
119 Gardner et al. (2013) on single-step decompression experiments supports the early work of
120 Walker and Mullins (1981), indicating a rather minor effect of the melt composition on the
121 surface tension of silicate melts and, thus, highlighting that further investigations are required.
122 However, following Hirth et al. (1970), the nucleation rate can be calculated using:

123 $$J = J_0 e^{\left[-\frac{\Delta G}{kT}\right]} \quad (1),$$

124 where J_0 is related to the statistical distribution of gas molecules in the melt, ΔG is the free
125 energy of formation of a critical nucleus, k is the Boltzmann constant and T is the temperature.
126 The nucleation pressure (P_N) characterizes the onset of nucleation in a melt at a specific
127 supersaturation pressure ΔP_N. Typically, the supersaturation pressure is lower in the event of
128 heterogeneous bubble nucleation than in the case of homogenous vesicle nucleation, owing to
129 reduced energy barriers (e.g., Hurwitz and Navon, 1994; Gardner and Denis, 2004; Iacono
130 Marziano et al., 2007; Larsen, 2008).
131 The growth of existing gas bubbles requires lower energies and can occur either by i) volatile
132 diffusion from the melt into adjacent preexisting bubbles or through ii) mechanical expansion
133 due to decreasing ambient pressure (e.g., Proussevitch et al., 1993; Sparks et al., 1994; Huber et
134 al., 2014). Bubble growth is kinetically preferred over bubble nucleation at lower degrees of
135 supersaturation, when the necessary nucleation pressure has not been reached yet. The growth
136 rate (G_R) is given by the increase of the bubble radius over a unit of time.

In natural magmatic systems crystals are certainly already present at magma storage conditions and, thus, heterogeneous nucleation is often expected (e.g., Mangan et al., 2004a). However, homogenous nucleation can also occur in low-crystalline magmas where high supersaturation of the interstitial bulk melt is reached before the volatiles can diffuse over the entire distance to bubbles that grow on sparsely distributed crystals. Moreover, only some specific crystals (probably oxides) may lead to heterogeneous bubble nucleation (see Section 4.2 and 4.4 for details and Hurwitz and Navon, 1994). Hence, magma composition and the prevailing pressure (P) – temperature (T) - oxygen fugacity (fO_2) conditions at depth significantly influence whether bubbles nucleate homogeneously or heterogeneously.

The rock vesicularity, the bubble size distribution (BSD) and the bubble number density (BND) have become the most important parameters in understanding and tracing volatile exsolution processes and their related magma ascent velocities. BSD refers to the number of bubbles per unit volume within a series of defined size intervals (typically shown in a histogram plot of population density vs. size; Marsh, 1988), whereas BND stands for the total number of bubbles per unit volume and can be described as (e.g., Toramaru, 1995; Gardner et al., 1999):

$$\mathrm{BND} = \frac{\phi_m}{\Sigma\left(\frac{n_i}{N_T} V_i\right)} \quad (2),$$

where ϕ_m is the vesicle volume fraction, N_T is the total number of bubbles, n_i is the bubble number and V_i is the bubble volume at a diameter i.

BNDs have been found to be strongly dependent on the decompression rate ($r = \Delta P/\Delta t$), particularly at fast ascent rates (e.g., Toramaru, 1995; 2006), showing a positive correlation between BND and ascent velocities. Higher BND values are an indicator for a large number of bubbles and, thus, are a record of dominating bubble nucleation over bubble growth (e.g., Mourtada-Bonnefoi and Laporte, 2004; Nowak et al., 2011). Furthermore, the volatile exsolution

and nucleation of gas bubbles is strongly dependent on the diffusivity of the volatile species in the melt. Thus, a possible delay in bubble nucleation can occur between a fast and a slow diffusing volatile component, affecting BND; see, e.g., difference in diffusion rates between H_2O and CO_2 in silicate melts studied by Baker et al. (2005). On the other hand, a sudden change to faster decompression rate can also lead to a second nucleation event in magmas with preexisting bubbles as experimentally investigated and modeled by Toramaru (2014) and others (e.g., Masotta et al., 2014). Here, secondary nucleation events result in complex, multi-peak BSD patterns (Toramaru, 2014) as observed in many studies on natural samples (Sparks and Brazier, 1982; Klug and Cashman, 1994; Klug et al., 2002; Formenti and Druitt, 2003; Polacci et al., 2003; 2008; Lautze and Houghton, 2007; Giachetti et al., 2010; Shea et al., 2010; Parcheta et al., 2013).

Additionally, the "bubble signature" of a rock can also be altered or overprinted by coalescence during an annealing period producing complex size distribution that might lead to the misinterpretation of multiple nucleation events (e.g., Masotta et al., 2014), or simply by volatile loss and separation upon degassing. Moreover, during and after degassing of a melt (within a magma), smaller bubbles are often removed by diffusive coarsening (Ostwald ripening) of the larger bubbles (Lautze et al., 2011). This process favors growth of larger bubbles, and once they reached a size of $\geq$ 1 mm they can ascent multiple kilometers within the magma reservoir. However, this bubble ascent takes hundreds to thousands of years as shown by Lautze et al. (2011) based on experimental results and, thus, cannot sufficiently explain the short delay observed at volcanic systems between seismic activity and volcanic gas release as well as the very fast release of gases prior or during eruptions (e.g., Hautmann et al., 2014). Here, the formation of tensile hydraulic fractures is probably the most plausible mechanism, which allows

rapid separation of a fluid from a magma and the transport of this fluid phase to the surface (Scandone et al., 2007; Hautmann et al., 2014).

2. Experimental techniques

2.1 Experimental devices

Most commonly, experimental studies on decompression-induced bubble formation focus on volcanic conduit regimes at relatively low pressures (≤ 500 MPa), representing relatively shallow depths (≤ 20 km). Such experiments are typically conducted in internally heated pressure vessels (IHPVs) or in cold-seal (externally heated) pressure vessels (CSPVs). Detailed description of their setup and mode of operation can be found in diverse publications (for IHPV: e.g., Holloway, 1971 and the review of Lofgren, 1987; for CSPV: e.g., Tuttle, 1949 and the review of Ulmer et al., 1987). The maximum pressure usually reaches up to 300 to 500 MPa, typically using argon (Ar) gas as the pressure medium. In some cases, CSPVs can have hydrothermal setups, using water for pressurization (H_2O-CSPV). TZM pressure vessels are a special type of cold-seal apparatuses that use a Mo-Ti-Zr-alloy for higher experimental run temperature (~1200 °C at 200 MPa), instead of the Waspaloy alloy and Rene 41 alloy in a standard CSPV (max. 850 °C at 300 MPa); see, e.g., Williams (1966) and Luth and Tuttle (1963). IHPV furnaces run conveniently at temperatures up to 1250 °C and pressures up to 500 MPa, while special high-temperature furnaces can reach 1450 °C and a pressure up to 900 MPa can be achieved in some IHPVs. The oxygen fugacity of experimental systems can be adjusted, for example, with i) the double-capsule technique by adding an outer capsule filled with a solid oxygen buffer (in H_2O- and Ar-IHPV or Ar-CSPV), or ii) via Ar-H_2 gas mixtures using a Shaw-membrane to monitor the H_2-partial pressure in IHPVs (e.g., Berndt et al., 2002), or iii) by using different alloys for the

vessel (in H_2O-CSPV). Sensor capsules are often used to determine the oxygen fugacity for a specific vessel/pressure-medium setup, especially if H_2 sensors are not available (e.g., Taylor et al., 1992). Quench rates are dependent on the applied technique (and the sample size). Simply switching off the power to the furnace in IHPVs or removing the hot autoclave from the external CSPV-furnace and cooling it off with compressed air results in quench rates of about 150-200 °C/min (e.g., Behrens and Zhang, 2009). Whereas the rapid-quench sample holders of IHPVs enable the capsule(s) to drop immediately into the colder part of the assembly (e.g., Holloway et al., 1992; Berndt et al., 2002), cooling the sample with ≥ 150 °C/sec. Similar quench rates can be achieved in vertical rapid-heat, rapid-quench (TZM) CSPV, which use a magnet to transfer the sample(s) between the hot and the cold zone (e.g., Gaillard et al., 2003).

Additionally, experimental techniques have been developed to observe bubble formation *in situ*, recording the nucleation and growth rates via digital video cameras and time-lapse photography. Most *in situ* observations setups are limited to atmospheric pressures, e.g., using a special furnace-setup at a X-ray beamline (Bai et al., 2008; 2011) or a heating stage on an optical microscope (e.g., Bagdassarov et al., 2000; Navon et al., 1998) or a moissanite cell apparatus (see, e.g., Schiavi et al. (2010) for detailed description). Efforts have been made to modify an internally heated vessel, adding a transparent sapphire window for *in situ* observation at high-temperatures and high-pressures (TIHPV; Gondé et al, 2006; 2011). This vessel design requires a high degree of maintenance and, thus, has unfortunately been abandoned (*Laporte and Gondé, personal correspondence*).

Decompression experiments in externally heated diamond anvil cells also allow *in situ* observation of bubble formation through, e.g., moissanite windows (Masotta et al., 2014). Here, the decompression rate is adjusted by (controlled) cooling of the sample chamber. Results of

such experiments are not directly comparable to isothermal decompression experiments owing to the strong influence of temperature on melt parameters such as viscosity and volatile diffusivity, which affected bubble formation, growth and coalescence.

For completion of the experimental device list, we want to mention decompression experiments performed in piston-cylinder apparatuses (PCA), simulating volatile degassing at greater depths corresponding to the lower mantle regime (e.g., Hardiagon et al., 2013). PCAs use steel pistons to compress a solid pressure medium surrounding the sample, reaching pressures up to several GPas. Cells are commonly made of, e.g., NaCl, BN, MgO and/or pyrex (e.g., Johannes et al., 1971). Gas pressure vessels (i.e., IHPV and CSPV) allow relatively large sample volumes and provide enough space for the capsule volume to expand owing to the formation of a fluid phase in the melt, while the gas pressure is measured directly by pressure transducers and gauges. Whereas in PCA experiments the sample pressure inside the apparatus has to be calibrated to the external oil pressure applied onto the steel pistons. Also there are concerns that at high decompression rates the oil pressure release is faster than the reaction (relaxation) time of the solid media around the capsule (*Hardiagon, personal correspondence*), leading to deviation of the pressure shown at the pressure transducer in relation to the true pressure on the sample (e.g., Boyd and England, 1960). Thus, additional calibrations are necessary, which can be quite challenging and time-consuming, and a constant decompression rate may not be possible.

In the following, we will focus on “shallow depth” decompression experiments, simulating the magma ascent from magma chamber depth (equivalent to 300-500 MPa) to near-surface pressures.

2.2 Capsule material and experimental design

The majority of the bubble nucleation experiments were conducted in gas or hydrothermal pressure vessels using Ar±H_2 gas mixtures or H_2O as a pressure medium. For these experiments, capsules suitable for magmatic pressures and temperatures are required (cf. Gondé et al., 2011; Fiege et al., 2014a). Here, Au is often the preferred material (e.g., Mangan et al., 2004a; 2004b), whereas other noble metal containers such as Pt and AuPd are also used (e.g., Gondé et al., 2011; Preuss et al., 2014), having the advantage to allow higher temperatures. However, the run durations are limited for Fe- and/or S-bearing compositions because the latter capsule materials form alloys with the Fe and S in the melt, which can lead to capsule failure (e.g., Barr and Grove, 2010; Zajacz et al., 2012; 2013; Fiege et al., 2015). A notable advantage of Au and Pt over AuPd (or even AgPd) alloy is certainly the high flexibility and elasticity of Au and Pt at high temperatures, which allows a better response to changes in pressure and, thus, also decreases chances of capsule failure (*pers. experience of the authors*).

Preliminary results of Preuss et al. (2014) indicate that using glass powder in the experimental setup instead of glass cylinders can lead to a ”preferred” bubble nucleation on former grain boundaries and more likely, on N_2-rich bubbles, which can form early during decompression owing to the low solubility (Carroll and Webster, 1994). Moreover, first results of Marxer et al. (2013) show that the capsule design can have a significant effect, at least on the shape of the bubbles. The fluid (and melt) density increases significantly during quenching, leading to a shrinkage (isometric contraction or deformation/flattening) or even a collapse of bubbles (Marxer et al., 2013; 2015). The bubbles stop to shrink at a fictive temperature that is possibly close to the glass transition temperature (T_g; Marxer et al., 2015). In experiments terminated using a rapid-quench technique the samples are typically cooled below the glass transition

temperature within a few seconds (e.g. Berndt et al., 2002). It should be emphasized that this quench related effect might be enhanced by the capsule design and material, since flat crimped run products of experiments performed in Au or Pt capsules typically do not show evidence of significant bubble deformation owing to quench related contraction (e.g., Hamada et al, 2010; Fiege et al., 2014a; 2015).

The undesired interaction of Fe and S of melt with the noble metal capsules, leading to Fe and S loss of the melt, can be avoided by using inner containers made out of, e.g., quartz (Fleet et al., 1991) or olivine (Beermann et al., 2011), which are suitable for high-temperature experiments at constant pressures. In these experimental setups a piston or lid is used to separate the melt inside the crystal container from an outer noble metal container. However, once pressurized these setups respond slowly and unpredictably to a pressure decrease in the vessel; i.e., continuous, controlled decompression is not possible (similar problem as for piston cylinder experiments). To our knowledge, successful decompression experiments using quartz, olivine or similar capsule materials do not exist.

Furthermore, as mentioned above, Masotta et al. (2014) performed experiments using a Bassett-type externally-heated diamond anvil cell, which allows *in situ* observation of bubble formation through moissanite windows. In these experiments, fluid-saturation and, thus, bubble formation is induced via rapid-cooling. The results provide valuable information, for example, about the required supersaturation pressure (ΔP_N) in different melt compositions (< 60 MPa in basalt and andesite; ~200 MPa in rhyodacite) and bubble growth rates. The experimental setup also allows the evaluation of the dominating degassing process (e.g., bubble growth vs. nucleation) at different stages of volatile exsolution. However, the sole effect of decompression rate (≈ magma ascent rate) cannot be tested by this experimental approach, since simultaneous cooling probably

affects significantly the bubble formation, growth and/or coalescence. For instance, heterogeneous bubble nucleation occurs simultaneously with crystal nucleation in the experiments of Masotta et al. (2014), which may have influenced supersaturation pressure ΔP_N and, hence, the degassing processes.

2.3 Starting composition

The majority of the published experimental studies were performed using evolved rhyolitic melt compositions at fluid-saturated conditions prior to decompression. Here, glass (drilled) cylinders or pieces of synthetic or natural glasses are typically hydrated in a first step (cf., Mourtada-Bonnefoi and Laporte, 2002). More recently the experimental community started to focus on less evolved systems (Mangan et al., 2004b; Cichy et al., 2011; Pichavant et al., 2013; Fiege et al., 2014a; Masotta et al., 2014). Here, Gondé et al. (2011) observed that water-undersaturated rhyodacitic melts may produce up to 3 log units higher BND than water-saturated ones at similar decompression rates, which seems to be consistent with experimental results of Fiege et al. (2014a) and Preuss et al. (2014). Considering that ($\pm CO_2$-free) natural systems are often not fluid-saturated prior to decompression, these observations are very important but certainly require further systematic experimental investigations.

2.4 Decompression style

Experimental studies on different pressure release techniques have emphasized the importance of the decompression paths on (homogeneous) bubble nucleation in melts (e.g., Nowak et al., 2011; Marxer et al., 2015). The three major styles used in literature are i) *single-step*, ii) *multi-step* and iii) *continuous decompression*; see Fig. 1. The single-step method simulates a scenario where the

entire magma ascent (from greater depths at the initial pressure P_i up to shallower depths at the final pressure P_f) is accomplished instantaneously within the first seconds of the experiments. Here, the subsequent annealing time (t_A) at final pressure determines the overall, integrated decompression rate ($r_{int} = \Delta P/\Delta t$; in this case corresponds to $[P_i-P_f]/t_A$). The multi-step method consists of a number of regular instantaneous pressure drops of fewer MPa followed by short-term annealing times at intermediate pressures until final experimental pressures have been reached and the experiment is quenched. In both cases the pressure release is typically conducted by manually opening needle valves to release the pressure medium (e.g., Ar gas or water) from the IHPV or CSPV. Whereas in a continuous decompression path no severe pressure drops occur but rather a controlled release of pressure at an uninterrupted manner. The sample is cooled immediately when the final pressure is reached (i.e., $t_A = 0$ h). Continuous pressure release has been mainly performed manually by opening a bleeding valve and monitoring the pressure on a strip chart recorder (e.g., Hamada et al., 2010), or can be done at very low decompression rates by issuing a piezoelectric-driven valve while visually controlling the values read from the pressure transducer with the number of ascending gas bubbles released into a water-filled glass column at the end of the pressure line (Nowak et al., 2011). Another possible way to perform experiments at constant decompression rates includes connecting two (or more) gas pressure vessels (IHPV or CSPV) and adjusting the decompression rate via controlled cooling of the connected vessel(s) while running the sample in the other vessel at constant temperature. However, with this technique, the range of decompression rates (fast rates are not possible) and the total decompression ΔP is rather limited (see, e.g., Waters, 2013); i.e., the pressure may only be decreased by a factor of ~2 via cooling of a connected "empty" vessel.

The study of Nowak et al. (2011) shows that homogeneous bubble nucleation is the dominant bubble forming process during a single-step pressure release (large number of relatively small bubble sizes, leading to a large BND), while bubble growth is dominating in continuously released water-saturated rhyodacitic melts (low bubble number density resulting from only few larger sized bubbles). A multi-step decompression technique can be seen as the intermediate case between the formerly discussed methods, where the predominance of either bubble nucleation or growth is mainly controlled by the number of reoccurring decompression-annealing steps, i.e., by the step size of the individual pressure drops.

In the results and discussion sections of this review article we will mainly focus on decompression experiments using continuous, constant decompression rates or multi-step approaches with very small steps (< 1 MPa), because of the better applicability to natural systems and the better reproducibility (see Section 4.6 and Marxer et al., 2015).

3. Analytical techniques

Chemical analyses of experimental run products are consulted in order to determine whether the volatile exsolution during decompression occurred in equilibrium or not. Especially very fast decompressed samples may end up having significantly higher contents of dissolved volatiles (e.g., H_2O, CO_2) in their residual melts in comparison to isobaric solubility experiments at final pressures. Mass balance calculations based on electron microprobe analysis (EMPA) datasets as well as Raman or Fourier transform infrared (FTIR) spectroscopy and Karl-Fischer titration are the most common techniques for water and carbon dioxide determination in the melt. Only few studies have made the effort to analyze the volatile content trapped inside the bubbles in order to calculate overpressures (e.g., CO_2-bubbles in mid-ocean ridge basalts; Burnard, 1999).

A very powerful tool for understanding bubble formation processes, their time-scales and relationship to eruption dynamics is the image and texture analysis of two- and three-dimensional vesicle features such as size, number and shape as well as nucleation and growth rates. Here, structural features such as interpenetration shapes, dimples or flattened inter-bubble melt films indicate a contribution of bubble coalescence (Castro et al., 2012). Textural analyses can be subdivided into two- and three-dimensional methods, which will be described separately in the following two sections.

3.1 2D methods

Two-dimensional (2D) digital images can be obtained by various techniques, e.g., optical or scanning electron microscopy, and are usually taken at various magnifications and locations to reduce truncation effects (= underestimation of the largest and/or the smallest bubbles; see Armienti, 2008). With the help of image processing programs (e.g., *ImageJ*; http://imagej.nih.gov/ij/) parameters such as area, width, length, and circularity of individual bubbles as well as the overall total area, average size and area fraction of vesicles throughout the images can be determined. The detection limit of single objects of interest is dictated by the magnification and resolution of the digital picture.

The next step is typically the stereological conversion of the two-dimensional results into three-dimensional (3D) information. The simplest approach is to assume perfectly shaped bubble spheres or, typically more appropriate, ellipsoidal shapes for vesicles of irregular (non-spherical) geometry, applying their general volume formulas and inserting these values into equations to determine population densities (n) used in bubble size distribution (BSD) plots, or to calculate bubble number densities (BND); see also Noguchi et al. (2008); Cichy et al. (2011).

The calculation of 3D bubble or particle distributions based on 2D information is complex and several approached were published within the last decades (e.g., Higgins, 1994; Peterson, 1996; Sahagian and Proussevitch, 1998). Computer programs have been created, which allow a (semi-) automatic stereological conversion of 2D into 3D data. Whereas the FOAMS software is limited to the assumption of spherical bubbles (Shea et al., 2010; http://www2.hawaii.edu/~tshea/foams/foamsintro.html), the CSDcorrection software by Higgins (2000, 2002, 2006, 2007; http://www.uqac.ca/mhiggins/csdcorrections.html) allows also the input of aspect ratio and circularity data of objects, reducing the stereological error and providing non-spherical bubble volumes presented in size distribution plots. Additionally, new ImageJ plugins have been made available that allow the easy data transfer into the CSDcorrection program. Higgins's software provides, for instance, the classic size distribution diagrams and corresponding tables; including the bubble number per size intervals, which give the BND when summed up.

3.2 3D methods

Within the last couple of years, non-destructive, high-resolution computer tomography (CT) or X-ray μ-tomography became popular among researchers studying natural and experimental rock textures. The main advantage of 3D-imaging is the resolution of possible bubble networks (e.g., owing to coalescence) and orientations that are otherwise not or not clearly visible in 2D-images. These tomographic scan datasets consist of 2D slice images, which can be individually processed as two-dimensional images as described in the previous section, or the entire set of images can be implemented into 3D computer programs. There is a number of commercially licensed 3D-software available, but also a couple of freeware, which are customized to the mineralogical

scope of texture analysis, e.g., BLOB3D (Ketcham, 2005; ftp://ftp.ctlab.geo.utexas.edu/Blob3D/) and YaDiV (Friese et al., 2013; http://www.welfenlab.de/yadiv.html). These programs allow the calculation of bubbles numbers and individual (true) bubble volumes via 3D-segmentation and separation of density-related grey values. Additionally, the segmented volumes of interest are visualized in 3D, which may unravel preferred orientation or flow structures that would have not been resolved with 2D-images only (see Fig. 2).

4. Results and Discussion of the experimental database

4.1 Supplementary decompression experiments

Recent studies indicate a significant effect of the melt composition on bubble formation and evolution during decompression (cf. Masotta et al., 2014; Fiege et al., 2014a). To further investigate the potential effect of (minor) volatile species such as S and Cl on the bubble number density during magma ascent, we performed three additional continuous decompression experiments for this review article, following the experimental and analytical strategy described by Fiege et al. (2014a); a more detailed description of the experiments is provided in Fiege et al. (2014b). We used the same anhydrous dacitic andesite as a starting material (see notes below Table A.1; appendix A).

In brief, the experimental procedure comprises three steps: 1) Synthesis of an anhydrous andesitic glass (1 atm; 1600 °C; 2 × 2 h); 2) Hydration (~6.2 wt% H_2O) of the glass in an internally heated pressure vessel (IHPV) at 1030 °C, 500 MPa for 12 h. Minor amounts of sulfur (~80 ppm) were added to the system using gypsum ($Ca[SO_4]$ $2H_2O$); 3) Continuous decompression experiments in an IHPV at 1030 °C. The initial pressure of the decompression experiments was 400 MPa. The pressure was released continuously at a constant decompression

435 rate of 0.1 MPa/s and the samples were quenched (rapid-quench technique) at final pressures of
436 150, 100 and 70 MPa. The synthesis and the decompression experiments were performed at
437 $\log(fO_2)$ = FMQ+3.6 (fayalite-magnetite-quartz buffer).
438 We collected five back scattered electron (BSE) images at different magnifications and locations
439 on each run product (selected images are shown in Fig. A.1; appendix A) and analyzed the
440 images following the procedure described by Fiege et al. (2014a). All relevant details for the
441 experiments as well as the BND values obtained for each run product are given in Table A.1 (see
442 appendix A). The analytical results of these additional run products are compared to literature
443 data and discussed in the following sections.
444

445 **4.2 Homogeneous vs. heterogeneous bubble nucleation**

446 Bubble nucleation in melts and magmas can be homogeneous or heterogeneous. Homogeneous
447 bubble nucleation requires relatively high supersaturation pressures ($\Delta P_N = P_N - P_{SAT}$; P_N:
448 nucleation pressure; P_{SAT}: volatile-saturation pressure) and typically occurs in systems without
449 phases that can serve as preferential nucleation sites (Hurwitz and Navon, 1994). Mangan et al.
450 (2004a) showed, based on numerical modeling using available experimental data that
451 heterogeneous bubble nucleation is trigged in water-saturated rhyolite at supersaturation
452 pressures ΔP_N < 5-20 MPa, while a supersaturation pressure of > 120-150 MPa is required for
453 homogeneous nucleation.
454 The interaction between crystals and heterogeneously forming (bubble-) nuclei is illustrated in
455 Fig. 3. It is emphasized that the sketched Fe-(Ti)-oxides in Fig. 3, serving as preferred nucleation
456 sites, are to be seen as examples. Even though, to our knowledge, only Fe-(Ti)-oxides have been
457 proven to trigger heterogeneous nucleation (e.g., Hurwitz and Navon, 1994; Cluzel et al., 2008),

458 other oxides such as hematites (e.g., Gardner and Denis, 2004; Gardner, 2007) and magnetites
459 (Edmonds et al., 2014; Knipping et al., 2015), but also (noble) metals (e.g., Mangan and Sisson,
460 2000) or even sulfides (Mungall et al., 2015) may have a similar effect. For instance,
461 experimental data from Matveev and Ballhaus (2002) indicate that the presence of chromites
462 probably favors heterogeneous bubble nucleation, while silicates such as plagioclase may have a
463 minor or even no effect (e.g., Cichy et al., 2011). According to Hurwitz and Navon (1994) a flat
464 interface between bubble and melt is formed when the wetting angle (Ψ) reaches 135° ($\Psi = 180° - \theta$; θ is the contact angle; the correct determination of wetting and contact angles can be found in
465
466 Gualda and Ghiorso; 2007). Here, the wetting angle can be used to calculate the wetting factor
467 (Φ), which is required to calculate supersaturation pressures for heterogeneous bubble nucleation
468 (see equations shown in Fig. 3); i.e., $\Phi = 1$ for homogeneous nucleation ($\Psi = 0°$). Hurwitz and
469 Navon (1994) showed that the supersaturation pressures can decrease down to ~1 MPa in
470 hydrous rhyolites, which contain Fe-Ti-oxide microlites and this was recently confirmed by *in*
471 *situ* observation of Masotta et al. (2014) using a diamond-anvil apparatus.
472 It is worth noting that heterogeneous bubble nucleation usually also occurs in experiments
473 ultimately designed to investigate homogeneous nucleation processes. Here, numerous but small
474 bubbles often form within a tiny layer (= fringe) of ≤ 10 μm at the melt-capsule interface. These
475 bubbles are often referred to as "fringe" bubbles (cf. Mangan and Sisson, 2000) and have to be
476 excluded for the determination of BND, BSD, etc.
477 For homogeneous bubble nucleation a negative correlation between the supersaturation pressure
478 and the initial H_2O content in the melt was observed by Mourtada-Bonnefoi and Laporte (2002),
479 while the supersaturation pressure was found to increase with increasing CO_2 concentration. This
480 is directly related to changes in volatile-saturation pressure , i.e., to the influence of pressure on

H_2O and CO_2 solubility in the silicate melts (e.g., Burnham, 1975; Holtz et al., 1992; Moore et al., 1995; Jakobsson, 1997; Shishkina et al., 2010; Lesne et al., 2011a, 2011b, 2011c).

In the following sections we will present and evaluate experimental results for homogeneous und heterogeneous bubble nucleation, respectively. As mentioned previously, we will mainly focus on experimental studies using continuous or almost continuous (e.g., multi-step decompression with small step sizes) decompression rates for the experiments. The set of available data (homogeneous and heterogeneous) is listed in Table 1 (all known bubble nucleation studies using continuous decompression technique are considered; selected studies using single- or multi-step technique are listed, too).

4.3 Available data for homogeneous bubble nucleation

Understanding bubble number density related to homogeneous bubble nucleation in silicate melts during continuous decompression has been the objective of ten experimental studies published in the last ~15 years. While the majority of these studies focuses on evolved rhyolitic compositions (six studies), experimental data on decompression-induced homogenous bubble nucleation in less evolved systems are very limited (see Fig. 4). Two relevant studies were published using intermediate melt compositions (rhyodacite: Gondé et al., 2011; andesite: Fiege et al., 2014a) and two using mafic melt composition (phonolite: Marxer et al., 2015; basalt: Pichavant et al., 2013). Additionally, Masotta et al. (2014) use rhyolitic, andesitic and basaltic compositions; however, the bubble nucleation in the studied systems is related to cooling and, thus, not directly comparable; i.e., the cooling-induced crystallization can change the degassing mechanism from homogeneous to heterogeneous.

Fig. 4a shows a compilation of the available experimental data, while Fig. 4b represents an enlarged view of 4a, focusing on BND values obtained at 800 °C for initially volatile-saturated rhyolite melts, containing variable amounts of CO_2 (0 to ~800 ppm). Notably, experimental results for decompression rates ≤ 0.02 MPa/s are very limited. The model of Toramaru (2006; see Section 5.1) is used to predict a trend for rhyolitic compositions at 800 °C. Although some datasets scatter significantly and (possible) effects of volatile contents and (anhydrous) melt composition have to be considered for a qualitative interpretation, the results indicate that for rhyolitic compositions the influence of temperature on BND may be rather small in the range of 700 to 1000 °C, which is consistent with observations made by Gondé et al. (2011) for rhyodacite.

On the other hand, melt composition seems to play a more significant role (e.g., Bai et al., 2008; Gondé et al., 2011; Fiege et al., 2014a; Masotta et al., 2014). Here, the compositional effect can be subdivided into effects related to significant changes in major element composition (e.g., from rhyolite to basalt) and effects related to changes in volatiles/fluid composition (e.g., variations in relative concentrations of H_2O, CO_2, S and Cl). For instance, for a given decompression rate, the bubble number density seems to increase by about two log unit from (evolved) rhyolitic to (primitive) basaltic melt compositions (see Fig. 4). Moreover, a positive correlation is observed between BND and CO_2 content. Here, the addition of ~800 ppm CO_2 may lead to an increase of BND by more than one log units (see Fig. 4b). However, the relevant data scatter quite a bit and experiments at 1 atm. show that ≥ 880 ppm CO_2 are required to affect bubble nucleation to a significant extent (Bai et al., 2008).

Gardner (2012) performed homogeneous bubble nucleation experiments using a water-saturated phonolitic melt. The author applied an experimental technique, which includes a fast

526 decompression step (~4 MPa/s at 1150 °C or ~12 MPa/s at 875 °C) followed by 10 to 37 s of
527 annealing. Therefore, the results are probably not directly comparable to continuous
528 decompression experiments, which are followed by immediate rapid-quench (cf., Nowak et al.,
529 2011). However, while the highly variable BND values that Gardner (2012) obtained for 875 °C
530 [$\log(BND \cdot mm^3) = 1.4$ or 4.6] are somewhat hard to interpret, the BND values determined for
531 1150 °C (average $\log(BND \cdot mm^3) = 2.0 \pm 0.6$) are obviously very low for an integrated
532 decompression rate of ~4 MPa/s when compared to the compiled data shown in Fig. 4. This
533 indicates that the effect of melt composition on BND is possibly inversed if a melt is fluid-
534 saturated (instead of fluid-undersaturated) prior to decompression conditions [*please note:* the
535 only relevant experimental results on non-rhyolitic compositions are based on experiments using
536 water-undersaturated starting glasses (Gondé et al., 2011; Pichavant et al., 2013; Fiege et al.,
537 2014a)]. Although, a more reasonable explanation for the low BND values found by Gardner
538 (2012) at 1150 °C in phonolitic systems is that the decrease in BND with annealing after
539 decompression is much more significant in less evolved, mafic (phonolitic) systems at 1150 °C
540 than in intermediate (andesitic) systems at 1030 °C (see Fig. 6 and Section 4.4), owing to higher
541 diffusivity and lower melt viscosities. The compositional effects on homogeneous bubble
542 nucleation are further discussed in Section 5.1.
543
544 **4.4 Available data for heterogeneous bubble nucleation**
545 There are five experimental studies on heterogeneous bubble nucleation using (almost)
546 continuous and constant decompression rates in their experimental setup (Mangan and Sisson
547 2000; Mangan et al, 2004a; 2004b; Cluzel et al., 2008; Cichy et al., 2011). Notably, to date, the
548 effect of the decompression technique (continuous, multi-, single-step) has only been studied for

549 homogeneous bubble nucleation (Nowak et al., 2011; Marxer et al., 2015). Thus, although the
550 main focus of this paper is to review results of continuous decompression experiments, Fig. 5
551 includes also results from three of the most comprehensive studies using single- (Gardner and
552 Denis, 2004; Gardner, 2007) or multi-step (Cichy et al., 2011) approaches in order to evaluate
553 the possible effect of changing decompression style on heterogeneous bubble nucleation. The
554 results from single- (or multi-) step experiments (Fig. 5a) clearly show that temperature and
555 decompression rate have small to negligible influence on BND. In contrast, in crystal-poor
556 rhyolitic systems at 800 to 900 °C, a strong positive correlation between BND and
557 decompression rate can be observed if a continuous decompression technique is applied, while
558 the effect of temperature may also be negligible [Fig. 5b; compare data from Mangan and Sisson
559 (2000) to results from Cluzel et al. (2008)]. This behavior is very similar to what can be observed
560 for homogeneous bubble nucleation (see Section 4.3; Fig. 4), as already noted by Mangan and
561 Sisson (2000), and indicates that degassing of rhyolitic magmas is rather controlled by
562 homogeneous than heterogeneous nucleation if the crystal content is below a certain threshold
563 ($<<$ 1 vol% or $\leq 10^4$ crystals/cm^3). On the other hand, a significant temperature-dependence can
564 be observed for the bubble formation in Fe-(Ti)-oxides-bearing runs (see Fig. 5b). Here, a strong
565 positive correlation between BND and decompression rate at 950 °C is indicated by the data of
566 Mangan et al. (2004a), while at lower temperatures (~850 °C) this effect is again rather small
567 (Mangan et al., 2004b). At 850 °C a change in bulk composition from rhyolitic to rhyodacitic
568 and, thus, a further increase in total crystal content, may also have a minor effect. Notably, the
569 run products of Cichy et al. (2011) contain only very small amounts of Fe-(Ti)-oxides (< 0.1
570 vol%), while the total crystal fraction ranges between ~1 and ~9 vol%, indicating that minerals
571 such as amphibole, clinopyroxene, orthopyroxene and/or plagioclase, which are present in

varying abundances in the experiments of Cichy et al. (2011), may change the degassing mechanism from dominantly homogeneous to dominantly heterogeneous bubble nucleation. Furthermore, the results for rhyolitic to rhyodacitic Fe-(Ti)-oxides-bearing systems at 850 °C are almost indistinguishable from those using multi- or single-step technique, indicating that such systems can be studied using multi- or single-step approaches without risking "artificial" (unnatural) effect.

4.5 The effect of annealing after decompression

There are several studies using a single-step decompression approach followed by various times of annealing. However, to our knowledge, only the study of Fiege et al. (2014a) applies the continuous decompression technique to investigate the influence of subsequent annealing on (homogeneous) bubble nucleation and evolution in andesitic melts at 1030 °C. The results show that BND decreases by ≥1 log unit during the first ~5 h of annealing (Fig. 6a). Based on the total duration of the experiment after initiation of the decompression and the total decrease in pressure, we have calculated the integrated decompression rate (r_{int}) for the experiments shown in Fig. 6a. In Fig. 6b we compare the results shown in Fig. 6a but using the integrated decompression rate, to the continuous decompression experiments by Fiege et al. (2014a) without annealing but at various decompression rates. Fig. 6b reveals that significant difference may be observed for experiments annealed for 1 to 5 h after fast decompression, while experiments annealed for ≥ 72 h seem to produce similar BND values at a given (integrated) decompression rate. These observations have two main implications:

i) A simple approach using a relatively fast decompression rate (~0.1 MPa/s) in a first stage followed by long term annealing (≥ 72 h) at final pressure in a second stage should produce

similar BND than an experiment based a continuous decompression approach with a rate identical to the integrated decompression rate used for the two-stages setup. This observation is of high importance for the design of future experiments since an almost constant and fast decompression rates of ≥ 0.1 MPa/s can be easily adjusted by simply bleeding gas out of a CSPV or IHPV via a manual valve; i.e., a special low-flow rate decompression valve is not necessarily required.

ii) Average magma ascent rates are often estimated based on a distinct seismic activity prior to eruption, the time of eruption and geophysical data constraining the approximate depth of the magma source (e.g., Shimizu et al., 1997; Cashman, 2004; Scandone et al., 2007; Castro and Dingwell, 2009; Sparks et al., 2012; Jousset et al., 2013). Here, magmas ascend with a velocity of > 10 km/h during Plinian eruptions, while the ascent rate for Volcanian eruptions is probably < 0.1 km/h. The high kinetic energy of magmas traveling upwards at > 10 km/h may easily allow it to overcome most obstacles along the conduit; i.e., the magma ascends almost continuously to the surface. On the other hand, magmas, which are characterized by significantly lower kinetic energy during eruption (i.e., much lower ascent rates), may easily stop ascending or slow down considerably for a certain amount of time before continuing to ascend to the surface. Here, the results presented in Fig. 6a indicate that such an intermittent ascent does not affect the final vesiculation of the volcanic ejecta if the average (integrated) ascent rates are ≤ 0.001 MPa/s (± Volcanian eruptions: Cashman, 2004).

4.6 The effect of decompression path on bubble forming processes

In general, bubble number densities produced by single-step and multi-step (depending on step size) runs can be orders of magnitude higher than BND of continuous style decompression

618 experiments at a given (integrated) decompression rate (Nowak et al., 2011; Marxer et al., 2015).
619 This has to be considered for the interpretation of BND values of natural samples based on
620 experimental results. We think that in volcanic systems two decompression/ascent scenarios are
621 most likely:
622 i) A magma starts to ascend along the conduit and moves all the way towards the surface without
623 major interruptions, which would result in a continuous decompression at a quite constant
624 decompression rate. These eruptions are most appropriately simulated by continuous
625 decompression experiments.
626 ii) A magma starts to ascend but the upwelling is interrupted at a certain place (or places) along
627 the conduit; i.e., the kinetic energy of the magma, related to buoyancy, does not allow it to
628 overcome an obstacle. Here, after decompression, which can induce degassing (depending on
629 volatile contents and total pressure decrease ΔP), the magma may remain for a certain time (=
630 annealing time) at certain pressure-temperature conditions before it (may or may not) continues
631 to ascend to the surface. Similar degassing processes can be induced if a magma volume from a
632 deeper reservoir ascends and intrudes into a shallower reservoir, assuming that the change in
633 pressure is sufficient to reach volatile-saturation. The vesiculation within such magmas at
634 relatively shallow depth is most appropriately simulated by continuous decompression
635 experiments, which are annealed for certain times after decompression at final pressure-
636 temperature conditions.
637 While scenario i) is more likely in Subplinian to Plinian eruptions were the momentum of an
638 ascending magma is high enough to overcome possible obstacles, a rather slowly ascending
639 magma might get stuck on its way to the surface. Here, fluid-melt disequilibrium conditions
640 related to fast (Plinian style) decompression can lead to overpressurization within the upwelling

641 melt/magma and, thus, may result in more explosive volcanic eruptions (e.g., Mangan and
642 Sisson, 2000). In agreement with recent results of Marxer et al. (2015), we strongly recommend
643 to use only continuous or almost continuous (step size < 1 MPa) decompression techniques,
644 which also improves the reproducibility of the experiments (Marxer et al., 2015).
645

646 ## 5. Implications for natural systems

647 ### 5.1. Compositional effects and decompression-rate-meter(s)

648 Toramaru (2006) developed a model, which allows one to predict the bubble number density for
649 a given decompression rate and, thus, is a valuable tool to estimate decompression rates (≈
650 magma ascent rates) based on the vesiculation of natural samples (e.g., pumices). Here, the
651 following equation based on numerical simulations of Toramaru (1995, 2006) and provided by
652 Hamada et al. (2010) can be used to predict BND:

653 $$\mathrm{BND} \approx 34 \cdot C_{SAT} \cdot \left(\frac{16 \cdot \pi \cdot \sigma_{LB}^3}{3 \cdot k \cdot T \cdot P_{SAT}^2} \right)^{-2} \cdot \left(\frac{\Omega_L \cdot P_{SAT}}{k \cdot T} \right)^{-\frac{1}{4}} \cdot \left(\frac{P_{SAT}^2 \cdot k \cdot T \cdot C_{SAT} \cdot D_{H2O}}{4 \cdot \sigma_{LB}^2 \cdot r} \right)^{-\frac{3}{2}} \quad (3),$$

654 where C_{SAT} is the H_2O content at saturation pressure expressed as the number of H_2O-molecules
655 per unit volume of liquid, σ is the surface tension of the bubble-liquid interface in N/m, k is the
656 Boltzmann constant (1.38×10^{-23} J/K), T is the temperature in K, P_{SAT} is the H_2O-saturation
657 pressure in Pa, Ω_L is the molecular volume of H_2O in the liquid (typically fixed to 3×10^{-29} m^3;
658 Toramaru 1989; Hamada et al. 2010), D_{H2O} is the H_2O diffusivity in the melt in m^2/s, and r is the
659 decompression rate in Pa/s. The surface tension of the bubble-liquid interface σ can be estimated
660 using the following equation 4 (e.g., Hirth et al. 1970; Blander and Katz 1975; Hurwitz and
661 Navon 1994; Mangan and Sisson 2005; Gardner and Ketcham 2011):

$$J = \frac{2 \cdot n_0^2 \cdot \Omega_L \cdot D_{H2O} \cdot [\sigma_{LB}/(k \cdot T)]^{1/2}}{a_0} \cdot \exp\left[\frac{-16 \cdot \pi \cdot \sigma_{LB}^3}{3 \cdot k \cdot T \cdot \Delta P^2}\right] \quad (4),$$

where J is the nucleation rate, which is calculated by dividing the BND by the time allowed for nucleation (t_N; see, e.g., Gardner and Ketcham 2011).

While this model reproduces experimental data of H_2O-saturated rhyolitic melts relatively well, it fails to reproduce H_2O-undersaturated melts and/or less evolved melt compositions (Gondé et al., 2011; Fiege et al., 2014a). The H_2O-undersaturated andesitic melts are characterized by 1-2 log units higher BND values at a given decompression rate when compared to H_2O-saturated rhyolitic melts. Moreover, the model of Toramaru (2006) does not consider the possible effect of variation in volatile composition on bubble nucleation. It has been noted that CO_2 affects bubble nucleation to a significant extent if the system contains ≥ 880 ppm CO_2 (cf. Bai et al., 2008) and that the diffusivity of carbon dioxide in the melt can limit CO_2 exsolution and, thus, restrict bubble growth (see Pichavant et al., 2013). The available experimental dataset indicates that even small amounts of CO_2 (< 800 ppm) might change BND considerably (Fig. 4b); however, more experiments are needed to allow modeling the effect of CO_2. Furthermore, although Fiege et al. (2014a) observed no dependence of BND on changing bulk S (from ~150 to ~1000 ppm) and Cl (0 to 1000 ppm), it cannot be ruled out that these volatiles can have a significant influence, considering that the S and Cl contents were not varied systematically and that the possible effects of S and Cl may be overprinted by smaller variations in the initial H_2O content (see Table 2 in Fiege et al., 2014a). Here, a comparison of the results of this study obtained for CO_2-Cl-free, S-poor dacitic andesite (average BND = $10^{5.4}$ mm^3) with the BND values determined by Fiege et al. (2014a) for CO_2-free, S-Cl-bearing dacitic andesite (BND = $10^{4.6}$ mm^3) at the same decompression rate (0.1 MPa/s), indicates a decrease of BND with the addition of Cl and/or S for

a given decompression rate. Hence, we suggest that the H_2O diffusivity term in equation 3 and 4 should be replaced by:

$$D_{vol+alk} = F_{H2O}\, D_{H2O} + F_{CO2}\, D_{CO2} + F_S\, D_S + + F_{Cl}\, D_{Cl} + F_{Na}\, D_{Na} \quad (5),$$

where F is the fraction of H_2O, CO_2, S, Cl and Na in the fluid, and D is the diffusivity of the respective molecule or element in the melt. Sodium should be considered since it is typically the charge-balancing cation for Cl within the fluid phase (e.g., Bodnar et al., 1985). A similar approach should be used for the molecular volume of H_2O in the liquid Ω_L. Here, a bulk value should be estimated for Ω_L based on the fluid composition. However, more experimental data are needed to calibrate the effect of varying volatile compositions on BND and to adjust equation 3, 4 and 5 accordingly.

While the proposed approach should help to improve applicability of equation 3 and 4 to more complex melts containing different volatile species it does not account for the influence of water activity a(H_2O) on BND at a given decompression rate as observed by Gondé et al. (2011) and Fiege et al. (2014a). Assuming that the ~800 ppm CO_2 in the experiments of Pichavant et al. (2013) and the minor amounts of S and Cl in some of the experiments of Fiege et al. (2014a) have a minor effect on BND, we can use these results in combination with the H_2O-undersaturrated experiments of Martel and Bureau (2001) and Gondé et al. (2011) to evaluate the effect of the water activity on bubble nucleation in CO_2-poor systems. Fig. 7 shows the relevant data. It is emphasized that Gondé et al. (2011) detected a water loss during their experiments, which depends on samples size and run duration. They showed that for shorter run duration of ~1000 s this effect is rather small. Thus, only runs 44, 45 and 51 are shown in Fig. 7 (run duration < 1400s; see Table 3 in Gondé et al., 2011).

It seems to be well-accepted that – for a given melt composition and given pressure-temperature conditions – the correlation between BND and decompression rate on a double logarithmic scale can be described by linear trends with a constant slope (e.g., Toramaru, 2006; Gondé et al., 2011; Fiege et al., 2014a). Hence, we propose that the following equation can be used to describe the relationship between the decompression rate r and BND in a simple way:

$$\log(\mathrm{BND}) = A \cdot \log(r) + B \quad (6),$$

where A and B are empirical parameters. Here, A is the slope of the linear trend(s), which according to Fiege at al. (2014a) is well predicted by the Toramaru (2006) model and A is estimated to be ~1.5, being in agreement with several previous studies (see trends in Fig. 4a). B is the Y-axis intersect, which can be easily calculated based on the known values for decompression rate and BND for each experimental data-point.

Since the experimental dataset is growing but still very limited (e.g., systematic investigations of the influence of major element composition, volatile contents and temperature on decompression-induced bubble formation are missing), we suggest that a model approach for the estimation of B in equation 6 should be kept relatively simple using only one well-constrained parameter, which varies with temperature and melt composition.

A melt property parameter, which is influenced by bulk composition and temperature, and which is directly affecting bubble formation is the melt viscosity (η). The viscosity of the most relevant silicate melts is experimentally very well constrained and different (numerical) model approaches exist, which allow us to accurately calculate the viscosity for various melt compositions and conditions. We emphasize that the diffusivities of volatiles such as H_2O, Cl, CO_2 and S can typically be well-described by the Eyring equations, which relates chemical diffusivities to melt viscosities (e.g., Behrens and Stelling, 2010; Zhang and Ni, 2010) and also

729 that the surface tension of a melt/liquid is closely related to its viscosity (e.g., Gardner and
730 Ketcham, 2011). We use the viscosity models of Hui and Zhang (2007) and of Giordano et al.
731 (2008), which are two of the most comprehensive and accepted models published in the last
732 couple of years. Notably, these models do not account for the effect of CO_2, S and Cl on
733 viscosity; however, these and other volatiles (Br, I) appear to be less important in terms of
734 directly influencing melt viscosity when compared to, e.g., H_2O (e.g., Dingwell and Hess, 1998;
735 Bourgue and Richet, 2001; Zimova and Webb, 2006; 2007; Giordano et al, 2008). The melt
736 viscosities were estimated for compositions prior to decompression and the average values for
737 the melt viscosities, calculated based on the two applied viscosity models, are provided in the
738 legend of Fig. 7. In Fig. 7b we plot the Y-axis intercept estimated for each relevant data-point or
739 -set assuming a slope of 1.5 (= A in equation 6; see above) against the predicted melt viscosity
740 (*please note:* average B values are presented in Fig. 7b for the results of Fiege at al. (2014a) and
741 Pichavant et al. (2014) as well as for results of Martel and Bureau (2001) at 750 °C). In a first
742 approach we fitted a logarithmic regression to describe the dependence between B and melt
743 viscosity η (equation 7):

744 $$B = -4.567\ (\pm 0.539) \cdot \log(\eta) + 7.876\ (\pm 0.299) \qquad (R^2 = 0.935) \qquad (7).$$

745 In combination with equation 6 the decompression rate r can be predicted based on bubble
746 number densities measured in natural samples, which were produced by the eruption of an
747 initially water-undersaturated magma. Although, considering that CO_2, S, and Cl may have a
748 significant effect on BND at a given decompression rate, equation 8 is proposed for CO_2-, S-,
749 and Cl-free systems. Here, the results of Pichavant et al. (2013; CO_2-bearing) and Fiege et al.
750 (2014a; S- and Cl-bearing) are excluded for the calculation of equation 8, while the results of this
751 study are still considered, since the starting glass contains only minor amounts of S (~80 ppm).

752 $B = -5.097\ (\pm 1.193) \cdot \log(\eta) + 8.197\ (\pm 0.756)$ $(R^2 = 0.859)$ (8).

753 We emphasize that the proposed parameterizations are based on a limited dataset and strongly
754 encourage the community to calibrate the relationship between melt viscosity, decompression
755 rate and bubble number density based on additional experimental studies.

756

757 **5.2. Linking experimental results to natural samples: Perspective for future experiments**

758 Studying bubble nucleation, both experimentally and theoretically, is an undeniable prerequisite
759 to understand and interpret the vesiculation in volcanic ejecta such as pumices or tephra. In this
760 manuscript we have reviewed the available experimental dataset and techniques, while focusing
761 on bubble textures produced by (almost) continuous decompression experiments. Even though
762 the evaluation of the existing data shows that there is a dependence of the bubble number
763 densities on the decompression path and more importantly on the decompression rate, we see the
764 urgent necessity to widen the experimental database to more mafic melt compositions as well as
765 to lower decompression rates (<< 0.1 MPa/s). We suggest performing future decompression
766 experiments mostly by (almost) continuous pressure release as this seems to reflect a more
767 natural approach of simulating magma ascent on the laboratory scale. However, the compilation
768 of experimental data shows that low ascent rates (≈ low decompression rates) can be simulated
769 by using relatively fast and continuous decompression steps (~0.1 MPa/s) followed by a long
770 term annealing period (more than ~70 h). In any case, experimentalists should balance out
771 advantages and disadvantages of different capsule material and designs, and carefully separate
772 homogeneous from heterogeneous bubble nucleation in their run products. It is highly
773 recommended to apply new, high precision technologies in terms of image analysis as 3D-

774 tomographic scans can provide true bubble volumes, shapes and networks, and in respect of *in*
775 *situ* observations techniques at simultaneous high-temperatures and high-pressures.
776 Progress has been made in the last decades on understanding the difference between
777 homogeneous und heterogeneous bubble nucleation. Various studies, mainly on rhyolitic
778 systems, show that the presence of Fe-(Ti)-oxides can lead to heterogeneous bubble nucleation
779 upon decompression (e.g., Hurwitz and Navon, 1994). However, while crystals are inevitably
780 present in magmas, the crystal fraction (Mangan et al., 2004a) and the crystal types seem to
781 dictate the dominant nucleation mechanism; i.e., heterogeneous vs. homogeneous (see the
782 compilation of experimental result in Fig. 5b). In systems with low amounts of Fe-(Ti)-oxides,
783 distances between heterogeneously nucleating bubbles may be too large to transport the volatiles
784 to the bubbles before the total decompression ΔP reaches values, which allows homogeneous
785 nucleation. Moreover, owing to the lack of experimental data on possibly heterogeneous bubble
786 nucleation in crystal-bearing but Fe-(Ti)-oxides free systems, it is still not possible to state
787 whether homogenous or heterogeneous bubble nucleation is prevailing in magmatic systems.
788 However, if oxides (and possible sulfides) are the only phases that significantly affect the
789 nucleation mechanism, parameters such as oxygen fugacity (and sulfur fugacity) may be critical
790 since they significantly influence the stability of oxides (and sulfides). Hence, the total fraction
791 of crystals relevant for bubble nucleation processes influences strongly the degassing mechanism
792 and, thus, controls whether degassing occurs at greater depth (higher pressures) via
793 heterogeneous nucleation (low ΔP required) or near surface (lower pressures) via homogeneous
794 nucleation (high ΔP required). The latter process results most likely in explosive and potentially
795 hazardous eruptions.

Moreover, the evaluated experimental dataset shows that the effects of melt compositions on bubble number density are significant and have to be investigated more systematically. A main focus of future experimental studies could be the influence of water activity on bubble formation and growth, which seems to be significant and is of high importance to improve our understanding of degassing mechanisms at depth and during magma ascent, considering that magmatic systems are often not water-saturated prior to eruption (e.g., Hervig et al. 1989; Gardner et al. 1995). Finally, we have to investigate the differences between equilibrium and non-equilibrium volatile exsolution in regimes of closed- or open-system degassing, allowing us to predict the kinetics of volcanic eruptions from effusive to explosive activity (e.g., Pichavant et al., 2013; Cashman, 2014) and from slow to fast magma ascent.

6. Conclusion

In this manuscript we have mainly reviewed existing experimental and analytical methods associated with the vesiculation of silicate melts during decompression. We are highlighting gaps in the available experimental dataset that should be filled in the near future and describe advantages and disadvantages of the different experimental and analytical approaches that could be applied to perform such studies. There are four main observations and outcomes of this study:

1. Close attention has to be paid to capsule design and decompression techniques when comparing different experimental datasets. For instance, the simulation of natural magma ascent is probably best reproduced by experiments using foremost continuous pressure release techniques.

2. Variations in melt composition can significantly influence volatile exsolution and bubble forming processes. Even variations in the abundance of minor volatile species, e.g., Cl and/or S, show notable effects on the evolution of bubble number densities.
3. Based on literature data and results obtained from additional decompression experiments presented in this study, we propose a new decompression-rate-meter for initially water-undersaturated melts that links the melt viscosity in a simple approach to the decompression rate and the bubble number density.
4. Efforts have to be made to widen the range of experimental data on decompression-induced (equilibrium and disequilibrium) vesiculation, especially to intermediate and mafic melt compositions, as the available dataset is still limited. These data will allow one to improve the calibration of the suggested decompression-rate-meter as well as of previously published models.

Acknowledgements

The authors would like to thank C. Gondé, M. Hardiagon and D. Laporte for information on experimental devices and performance strategies provided via personal correspondence. We would like to thank J. Gardner and an anonymous reviewer for their comments and corrections, which helped to improve the manuscript. We are grateful to B. Konecke and J.L. Knipping for their helpful comments and remarks and to G. Zellmer for his editorial work.

References

Armienti, P. (2008) Decryption of igneous rock textures: crystal size distribution tools. In K.D. Putirka and F.J. Tepley III, Eds., Minerals, Inclusions and Volcanic Processes, 69, p. 623–

649. Reviews in Mineralogy and Geochemistry, Mineralogical Society of America, Chantilly, Virginia.

Audétat, A., and Simon, A.C. (2012) Magmatic controls on porphyry copper deposits. Society of Economic Geologists, Inc., Special Publication, 16, 573-618.

Bagdassarov, N., Dorfman, A., and Dingwell, D.B. (2000) Effect of alkalis, phosphorus, and water on the surface tension of haplogranite melt. American Mineralogist, 85, 33-40.

Bai, L., Baker, D.R., and Rivers, M. (2008) Experimental study of bubble growth in Stromboli basalt melts at 1atm. Earth and Planetary Science Letters, 267, 533-547.

Bai, L., Baker, D.R., Polacci, M., and Hill, R.J. (2011) In-situ degassing study on crystal-bearing Stromboli basaltic magmas: Implications for Stromboli explosions. Geophysical Research Letters, 38, L17309, doi: 10.1029/2011GL048540.

Baker, D.R., Freda, C., Brooker, R.A., and Scarlato, P. (2005) Volatile diffusion in silicate melts and its effects on melt inclusions. Annals of Geophysics, 48 (4/5), 699-717.

Barr, J.A., and Grove, T.L. (2010) AuPdFe ternary solution model and applications to understanding the fO_2 of hydrous, high-pressure experiments. Contributions to Mineralogy and Petrology, 160, 631-643.

Beermann, O., Botcharnikov, R.E., Holtz, F., Diedrich, O., and Nowak, M. (2011) Temperature dependence of sulfide and sulfate solubility in olivine-saturated basaltic magmas. Geochimica et Cosmochimica Acta, 75, 7612-7631.

Behrens, H., and Stelling, J. (2011) Diffusion and Redox Reactions of Sulfur in Silicate Melts. Reviews in Mineralogy and Geochemistry, 73, 79-111.

Behrens, H. and Zhang, Y. (2009) H_2O Diffusion in peralkaline to peraluminous rhyolitic melts. Contributions to Mineralogy and Petrology, 157, 765-780.

Berndt, J., Liebske, C., Holtz, F., Freise, M., Nowak, M., Ziegenbein, D., Hurkuck, W., and Koepke, J. (2002) A combined rapid-quench and H_2-membrane setup for internally heated pressure vessels: Description and application for water solubility in basaltic melts. American Mineralogist, 87, 1717-1726.

Blander, M., and Katz, J.L. (1975) Bubble nucleation in liquids. American Institute of Chemical Engineers Journal, 21, 833-848.

Bodnar, R.J., Burnham, C.W., and Sterner, S.M. (1985) Synthetic fluid inclusions in natural quartz. III. Determination of phase equilibrium properties in the system H_2O-NaCl to 1000 C and 1500 bars. Geochimica et Cosmochimica Acta, 49, 1861-1873.

Bourgue, E., and Richet, P. (2001) The effects of dissolved CO< sub> 2</sub> on the density and viscosity of silicate melts: a preliminary study. Earth and Planetary Science Letters, 193, 57-68.

Boyd, F.R., and England, J.L. (1960) Apparatus for phase-equilibrium measurements at pressures up to 50 kilobars and temperatures up to 1750°C. Jounral of Geophysical Research 65, 741-748.

Bluth, G.J.S., Doiron, S.D., Schnetzler, C.C., Krueger, A.J., and Walter, L.S. (1992) Global Tracking of the SO_2 Clouds from the June, 1991 Mount-Pinatubo Eruptions. Geophysical Research Letters, 19, 151-154.

Burnard, P. (1999) The bubble-by-bubble volatile evolution of two mid-ocean ridge basalts. Earth and Planetary Science Letters, 174, 199-211.

Burnham, C.W. (1979) Magmas and hydrothermal fluids. In H. L. Barns, Ed., Geochemistry of hydrothermal ore deposits, p. 71-136. John Willey and Sons, New York.

885 Carroll, M.R., and Webster, J.D. (1994) Solubilities of sulfur, noble gases, nitrogen, chlorine,
886 and fluorine in magmas. Reviews in Mineralogy and Geochemistry, 30, 231-279.
887 Cashman, K.V. (2004) Volatile controls on magma ascent and eruption. In R.S.J. Sparks and C.J.
888 Hawkesworth, Eds., The State of the Planet: Frontiers and Challenges in Geophysics, 150, p.
889 109-124. Geophysical Monograph series, American Geophysical Union, Washington.
890 Cashman, K.V. (2014) Petrological regime diagrams: Parameterizing kinetic controls on
891 vesiculation and crystallization. Abstract V43F-02 presented at 2014 Fall Meeting, AGU,
892 San Francisco, Calif., 15-19 Dec.
893 Castro, J.M., and Dingwell, D.B. (2009) Rapid ascent of rhyolitic magma at Chaitén Volcano,
894 Chile. Nature, 461, 780-783.
895 Castro, J.M., Burgisser, A., Schipper, C.I., and Mancini, S. (2012) Mechanisms of bubble
896 coalescence in silicic magmas. Bulletin of Volcanology, 74, 2339-2352.
897 Cluzel, N., Laporte, D., Provost, and A. Kannewischer, I. (2008) Kinetics of heterogeneous
898 bubble nucleation in rhyolitic melts: implications for the number density of bubbles in
899 volcanic conduits and for pumice textures. Contributions to Mineralogy and Petrology, 156,
900 745-763.
901 Cichy, S.B., Botcharnikov, R.E., Holtz, F., and Behrens, H. (2011) Vesiculation and Microlite
902 Crystallization Induced by Decompression: a Case Study of the 1991–1995 Mt Unzen
903 Eruption (Japan). Journal of Petrology, 52, 1469-1492.
904 Dingwell, D.B., and Hess, K.U. (1998) Melt viscosities in the system Na-Fe-Si-OF-Cl:
905 Contrasting effects of F and Cl in alkaline melts. American Mineralogist, 83, 1016-1021.

Edmonds, M., Aiuppa, A., Humphreys, M., Moretti, R., Giudice, G., Martin, R.S., Herd, R.A., and Christopher, T. (2010) Excess volatiles supplied by mingling of mafic magma at an andesite arc volcano. Geochemistry, Geophysics, Geosystems, 11, Q04005.

Edmonds, M., Brett, A., Herd, R.A., Humphreys, M.C.S. and Woods, A. (2014) Magnetite-bubble aggregates at mixing interfaces in andesite magma bodies. Geological Society, London, Special Publication, 410, SP410-7, doi: 10.1144/SP410.7.

Fiege, A., Holtz, F., and Cichy, S.B. (2014a) Bubble formation during decompression of andesitic melts. American Mineralogist, 99, 1052-1062.

Fiege, A. Behrens, H., Holtz, F., Adams, F. (2014b) Kinetic vs. thermodynamic control of degassing of H_2O–S+/-Cl-bearing andesitic melts. Geochimica et Cosmochimica Acta, 125, 241-264.

Fiege, A., Holtz, F., Behrens, H., Mandeville, C. W., Shimizu, N., Crede, L. S., and Göttlicher, J. (2015) Experimental Investigation of the S and S-Isotopes Distribution between H_2O-S±Cl Fluids and Basaltic Melts during Decompression. Chemical Geology, 393-394, 36-54.

Fleet, M.E., Stone, W.E., and Crocket, J.H. (1991) Partitioning of palladium, iridium, and platinum between sulfide liquid and basalt melt: Effects of melt composition, concentration, and oxygen fugacity. Geochimica et Cosmochimica Acta, 55, 2545-2554.

Formenti, Y., and Druitt, T.H. (2003) Vesicle connectivity in pyroclasts and implications for the fluidisation of fountain-collapse pyroclastic flows, Montserrat (West In-dies). Earth and Planetary Science Letters, 214, 561-574.

Friedlingstein, P., Houghton, R. A., Marland, G., Hackler, J., Boden, T. A., Conway, T. J., Canadell, J. G., Raupach, M. R., Ciais, P., and Le Quéré, C. (2010) Update on CO_2 emissions. Nature Geoscience, 3, 811–812. doi:10.1038/ngeo1022

Friese, K.-I., Cichy, S.B., Wolter, W.-E. and Botcharnikov, R.E. (2013) Analysis of tomographic mineralogical data using YaDiV – Overview and practical case study. Computer & Geosciences, 56, 92-103

Gaillard, F., Schimdt, B., Mackwell, S. and McCammon, C. (2003) Rate of hydrogen-iron redox echange in silicate melts and glasses. Geochimica et Cosmochimica Acta 67, 2427-2441.

Gardner, J.E. (2007) Heterogeneous bubble nucleation in highly viscous silicate melts during instantaneous decompression from high pressure. Chemical Geology, 236, 1-12.

Gardner, J.E. (2012) Surface tension and bubble nucleation in phonolite magmas. Geochimica et Cosmochimica Acta, 76, 93-102.

Gardner, J.E., and Denis, M.-H. (2004) Heterogeneous bubble nucleation on Fe-Ti oxide crystals in high-silica rhyolitic melts. Geochimica et Cosmochimica Acta, 68, 3587-3597.

Gardner, J.E., and Ketcham, R.A. (2011) Bubble nucleation in rhyolite and dacite melts: temperature dependence of surface tension. Contributions to Mineralogy and Petrology, 162, 929-943.

Gardner, J.E., Rutherford, M., Carey, S., and Sigurdsson, H. (1995) Experimental constraints on pre-eruptive water contents and changing magma storage prior to explosive eruptions of Mount St Helens volcano. Bulletin of Volcanology, 57, 1-17.

Gardner, J.E., Hilton, M., and Carroll, M.R. (1999) Experimental constraints on degassing of magma: istothermal bubble growth during continuous decompression from high-pressure. Earth and Planetary Science Letters, 168, 201-218.

Gardner, J.E., Ketcham, R.A. and Moore, G. (2013) Surface tension of hydrous silicate melts: Constraints on the impact of melt composition. Journal of Volcanology and Geothermal Research, 267, 68-74.

952 Gerlach, T.M., Westrich, H.R., and Symonds, R.B. (1996) Pre-eruption vapor in magma of the
953 climactic Mount Pinatubo eruption: Source of the giant stratospheric sulfur dioxide cloud.
954 In: Newhall, C.G., Punongbayan, R.S. (eds.), Fire and mud: Eruptions and lahars of Mt.
955 Pinatubo, Philippines, 415-433.
956 Giachetti, T., Druitt, T.H., Burgisser, A., Arbaret, L., and Galven, C. (2010) Bubble nu-cleation,
957 growth and coalescence during the 1997 Vulcanian explosions of Soufrière Hills Volcano,
958 Montserrat. Journal of Volcanology and Geothermal Research, 193, 215-231.
959 Gondé, C., Massare, D., Bureau, H., Martel, C., Pichavant, M., and Clocchiatti, R. (2006) In situ
960 study of magmatic processes: a new experimental approach. High Pressure Research, 26, 24-
961 250.
962 Gondé, C., Martel, C., Pichavant, M., and Bureau, H. (2011) In situ bubble vesiculation in silicic
963 magmas. American Mineralogist, 96, 111-124.
964 Giordano, D., Russell, J.K., and Dingwell, D.B. (2008) Viscosity of magmatic liquids: A model.
965 Earth and Planetary Science Letters, 271, 123-134.
966 Gualda, G.A., and Ghiorso, M.S. (2007) Magnetite scavenging and the buoyancy of bubbles in
967 magmas. Part 2: Energetics of crystal-bubble attachment in magmas. Contributions to
968 Mineralogy and Petrology, 154, 479-490.
969 Halter, W.E., Heinrich, C.A., and Pettke, T. (2005) Magma evolution and the formation of
970 porphyry Cu–Au ore fluids: evidence from silicate and sulfide melt inclusions. Mineralium
971 Deposita, 39, 845-863.
972 Hamada, M., Laporte, D., Cluzel, N., Koga, K.T., and Kawamoto, T. (2010) Simulating bubble
973 number density of rhyolitic pumices from Plinian eruptions: constraints from fast
974 decompression experiments. Bulletin of Volcanology, 72, 735-746.

975 Hardiagon, M., Laporte, D., Marizet, Y. and Provost, A. (2013) CO_2 degassing in a haplo-
976 basaltic magma: An experimental approach. Mineralogical Magazine, 77(5), 1258,
977 DOI:10.1180/minmag.2013.077.5.8
978 Hattori, K.H., and Keith, J.D. (2001) Contribution of mafic melt to porphyry copper
979 mineralization: evidence from Mount Pinatubo, Philippines, and Bingham Canyon, Utah,
980 USA. Mineralium Deposita, 36, 799-806.
981 Hautmann, S., Witham, F., Christopher, T., Cole, P., Linde, A.T., Sacks, I.S., and Sparks, R.S.J.
982 (2014) Strain field analysis on Montserrat (WI) as tool for assessing permeable flow paths in
983 the magmatic system of Soufrière Hills Volcano. Geochemistry Geophysics Geosystems, 15,
984 676-690.
985 Hervig, R.L., Dunbar, N., Westrich, H.R., and Kyle, P.R. (1989) Pre-eruptive water content of
986 rhyolitic magmas as determined by ion microprobe analyses of melt inclusions in
987 phenocrysts. Journal of Volcanology and Geothermal Research, 36, 293-302.
988 Higgins, M.D. (1994) Numerical modelling of crystal shapes in thin sections: Estimation of
989 crystal habit and true size. American Mineralogist, 79, 113-119.
990 Higgins, M.D. (2000) Measurement of crystal size distributions. American Mineralogist, 85,
991 1105-1116.
992 Higgins, M.D. (2002) Closure in crystal size distributions (CSD), verification of CSD
993 calculations, and the significance of CSD fans. American Mineralogist, 87, 171-175.
994 Higgins, M.D. (2006) Quantitative textural measurements in igneous and metamorphic
995 petrology. Cambridge University Press 10.2277/0521847826.

Higgins, M.D., and Chandrasekharam, D. (2007) Nature of Sub-volcanic Magma Chambers, Deccan Province, India: Evidence from Quantitative Textural Analysis of Plagioclase Megacrysts in the Giant Plagioclase Basalts. Journal of Petrology, 48, 885-900.

Hirth, J.P., Pound, G.M., and Pierre, G.R.St. (1970) Bubble nucleation. Metallurgical Transactions, 1, 939-945.

Holloway, J.R. (1971) Internally heated pressure vessels. In G.C. Ulmer and h.E. Barnes, Eds., Research techniques for high temperature and pressure, p. 217-257. Springer-Verlage, New York.

Holloway, J.R., Dixon, J.E., and Pawley, A.R. (1992) An internally heated, rapid-quench, high-pressure vessel, American Mineralogist, 77, 643-646.

Holtz, F., Behrens, H., Dingwell, D.B., and Taylor, R.P. (1992) Water solubility in aluminosilicate melts of haplogranite composition at 2 kbar. Chemical Geology, 96, 289-302.

Huber, C., Nguyen, C.T., Parmigiani, A., Gonnermann, H.M. and Dufek, J. (2014) A new bubble dynamics model to study bubble growth. Deformation, and coalescence. Journal of Geophysical Research: Solid Earth, doi: 10.1002/2013JB010419.

Hui, H., and Zhang, Y. (2007) Toward a general viscosity equation for natural anhydrous and hydrous silicate melts. Geochimica et Cosmochimica Acta, 71, 403-416.

Hurwitz, S., and Navon, O. (1994) Bubble nucleation in rhyolitic melts: Experiments at high pressure, temperature, and water content. Earth and Planetary Science Letters, 122, 267-280.

Iacono Marziano, G., Schmidt, B.C. and Dolfi, D. (2007) Equilibrium and disequilibrium degassing of a phonolitic melt (Vesuvius AD 79 “white pumice”) simulated by

1018 decompression experiments. Journal of Volcanology and Geothermal Research 161, 151-
1019 164.
1020 Jakobsson, S. (1997) Solubility of water and carbon dioxide in an icelandite at 1400°C and 10
1021 kilobars. Contributions to Mineralogy and Petrology, 127, 129-135.
1022 Johannes, W., Bell, P.M., Mao, H.K., Boettcher, A.L., Chipman, D.W., Hays, J.F., Newton, R.C.
1023 and Seifert, F. (1971) An Interlaboratory Comparison of Piston-Cylinder Pressure
1024 Calibration Using the Albite-Breakdown Reaction. Contributions to Mineralogy and
1025 Petrology, 32, 24-38.
1026 Jousset, P., Budi-Santoso, A., Jolly, A.D., Boichu, M., Surono, Dwiyono, S., Sumarti, S.,
1027 Hidayati, S. and Thierry, P. (2013) Signs of magma ascent in LP and VLP seismic events
1028 and link to degassing: An example from the 2010 explosive eruption at Merapi volcano,
1029 Indonesia. Journal of Volcanology and Geothermal Research 261, 171-192.
1030 Ketcham, R.A. (2005) Computational method for quantitative analysis of three-dimensional
1031 features in geological specimens. Geosphere, 1, 32-41, doi: 10.1130/GES00001.1.
1032 Klimont, Z., Smith, S.J., Cofala, J., 2013. The last decade of global anthropogenic sulfur dioxide:
1033 2000–2011 emissions. Environmental Research Letters 8.
1034 Klug, C., and Cashman, K.V. (1994) Vesiculation of May 18, 1980, Mount St. Helens magma.
1035 Geology, 22, 468-472.
1036 Klug C., Cashman K.V., and Bacon C.R. (2002) Structure and physical characteristics of pumice
1037 from the climatic eruption of Mount Mazama (Crater Lake), Oregon. Bulletin of
1038 Volcanology, 64, 486-501.

Knipping, J.L., Bilenker, L.D., Simon, A.C., Reich, M., Barra, F., Deditius, A.P., Lundstrom, C., Bindeman, I., and Munizaga, R. (2015) Giant Kiruna-type deposits form by efficient flotation of magmatic magnetite suspensions. Geology (in press), doi: 10.1130/G36650.1.

Lautze, N.C., and Houghton, B.F. (2007) Linking variable explosion style and magma textures during 2002 at Stromboli volcano, Italy. Bulletin of Volcanology, 69, 445-460.

Lautze, N., Sisson, T., Mangan, M., and Grove, T. (2011) Segregating gas from melt: an experimental study of the Ostwald ripening of vapor bubbles in magmas. Contributions to Mineralogy and Petrology, 161, 331-347.

Lesne, P., Kohn, S.C., Blundy, J., Witham, F., Botcharnikov, R.E., and Behrens, H. (2011a) Experimental simulation of closed-system degassing in the system Basalt-H_2O-CO_2-S-Cl. Journal of Petrology, 52, 1737-1762.

Lesne, P., Scaillet, B., Pichavant, M., and Beny, J.-M. (2011b) The carbon dioxide solubility in alkali basalts: an experimental study. Contributions to Mineralogy and Petrology, 162, 153-168.

Lesne, P., Scaillet, B., Pichavant, M., and Beny, J.-M. (2011c) The H_2O solubility in alkali basaltic melts: an experimental study. Contributions to Mineralogy and Petrology, 162, 133-151.

Lofgren, G. (1987) Internally Heated Systems. In G.C. Ulmer and H.E. Barnes, Eds., Hydrothermal Experimental Techniques, 523 pages, John Wiley and Sons, New York.

Luth, W.C., and Tuttle, O.F. (1963) Externally heated cold-seal pressure vessels for use to 10,000 bars and 750°C. American Mineralogist, 48, 1401-1403.

Manga, M., and Stone, H.A. (1994) Interactions between bubbles in magmas and lavas: effects of bubble deformation. Journal of Volcanology and Geothermal Research, 63, 267-279.

Mangan, M., and Sisson, T. (2000) Delayed, disequilibrium degassing in rhyolite magma: decompression experiments and implications for explosive volcanism. Earth and Planetary Science Letters, 183, 441-455.

Mangan, M., and Sisson, T. (2005) Evolution of melt-vapor surface tension in silicic volcanic systems: Experiments with hydrous melts. Journal of Geophysical Research, 110, B01202.

Mangan, M., Mastin, L., and Sisson, T. (2004a) Gas evolution in eruptive conduits: combining insights from high temperature and pressure decompression experiments with steady-state flow modeling. Journal of Volcanology and Geothermal Research, 129, 23-36.

Mangan, M.T., Sisson, T.W., and Hankins, W.B. (2004b) Decompression experiments identify kinetic controls on explosive silicic eruptions. Geophysical Research Letters, 31, L08605.

Marsh, B.D. (1988) Crystal size distribution (CSD) in rocks and the kinetics and dynamics of crystallization. Contribution to Mineralogy and Petrology, 99, 277-291.

Martel, C., and Bureau, H. (2001) In situ high-pressure and high-temperature bubble growth in silicic melts. Earth and Planetary Science Letters, 191, 115-127.

Marxer, H., Bellucci, P., Ulmer, S., and Nowak, M. (2013) Experimental magma degassing: The revenge of the deformed bubbles. American Geophysical Union, Fall Meeting 2013, abstract #V23E-02

Marxer, H., Bellucci, P., and Nowak, M. (2015). Degassing of H_2O in a phonolitic melt: A closer look at decompression experiments. Journal of Volcanology and Geothermal Research, in press, doi:10.1016/j.jvolgeores.2014.11.017

Masotta, M., Ni, H. and Keppler, H. (2014) In situ observations of bubble growth in basaltic, andesitic and rhyodacitic melts. Contributions to Mineralogy and Petrology, 167:967.

1084 Matveev, S., and Ballhaus, C. (2002) Role of water in the origin of podiform chromitite
1085 deposits. Earth and Planetary Science Letters, 203, 235-243.
1086 McGee, K.A., Doukas, M.P., Kessler, R. and Gerlach, T., 1997, Impacts of volcanic gases on
1087 climate, the environment, and people: U.S. Geological Survey Open-File Report 97-262, 2 p.
1088 Moore, G., Vennemann, T., and Carmichael, I.S.E. (1995) Solubility of Water in Magmas to
1089 2kbar. Geology, 23, 1009-1102.
1090 Mourtada-Bonnefoi, C.C., and Laporte, D. (1999) Experimental study of homogeneous bubble
1091 nucleation in rhyolitic magmas. Geophysical Research Letters, 26, 3505-3508.
1092 Mourtada-Bonnefoi, C.C., and Laporte, D. (2002) Homogeneous bubble nucleation in rhyolitic
1093 magmas: An experimental study of the effect of H_2O and CO_2. Journal of Geophysical
1094 Research, 107, ECV 2-1-EVC 2-19.
1095 Mourtada-Bonnefoi, C.C., and Laporte, D. (2004) Kinetics of bubble nucleation in a rhyolitic
1096 melt: an experimental study of the effect of ascent rate. Earth and Planetary Science Letters,
1097 218, 521-537.
1098 Mungall, J.E., Brenan, J.M., Godel, B., Barnes, S.J., and Gaillard, F. (2015). Transport of metals
1099 and sulphur in magmas by flotation of sulphide melt on vapour bubbles. Nature
1100 Geoscience, 8, 216-219.
1101 Namiki, A. (2012) An empirical scaling of shear-induced outgassing during magma ascent:
1102 intermittent magma ascent causes effective outgassing. Earth and Planetary Science Letters,
1103 353-354, 72-81.
1104 Namiki, A., and Manga, M. (2008) Transition between fragmentation and permeable outgassing
1105 of low viscosity magmas. Journal of Volcanology and Geothermal Research, 169, 48-60.

1106 Navon, D., Chekhmir, A. and Lyakhovsky, V. (1998) Bubble growth in highly viscous melts:
1107 theory, experiments, and autoexplosivity of dome lavas. Earth and Planetary Science Letters,
1108 160, 763-776.
1109 Noguchi, S., Toramaru, A., and Nakada, S. (2008) Relation between microlite textures and
1110 discharge rate during the 1991-1995 eruptions at Unzen, Japan. Journal of Volcanology and
1111 Geothermal Research, 175, 141-155.
1112 Nowak, M., Cichy, S.B., Botcharnikov, R.E., Walker, N., and Hurkuck, W. (2011) A new type
1113 of high-pressure low-flow metering valve for continuous decompression: First experimental
1114 results on degassing of rhyodacitic melts. American Mineralogist, 96, 1373-1380.
1115 Parcheta, C.E., Houghton, B.F., and Swanson, D.A. (2013) Contrasting patterns of vesiculation
1116 in low, intermediate, and high Hawaiian fountains: a case study of the 1969 Mauna Ulu
1117 eruption. Journal of Volcanology and Geothermal Research, 255, 79-89.
1118 Peterson, T. (1996) A refined technique for measuring crystal size distributions in thin section.
1119 Contributions to Mineralogy and Petrology, 124, 395-405.
1120 Pichavant, M., Di Carlo, I., Rotolo, S.G., Scaillet, B., Burgisser, A., Le Gall, N. and Martel, C.
1121 (2013) Generation of CO_2-rich melts during basalt magma ascent and degassing.
1122 Contributions to Mineralogy and Petrology, 166, 545-561.
1123 Polacci M., Pioli L., and Rosi, M. (2003) The Plinian phase of the Campanian Ignimbrite
1124 eruption (Phlegrean Fields, Italy): evidence from density measurements and textural
1125 characterization of pumice. Bulletin of Volcanology, 65, 418-432.
1126 Polacci, M., Baker, D.R., Bai, L., Mancini, L. (2008) Large vesicles record pathways of
1127 degassing at basaltic volcanoes. Bulletin of Volcanology, 70, 1023-1029.

Proussevitch, A.A., and Sahagian, D.L. (1996) Dynamics of coupled diffusive and decompressive bubble growth in magmatic systems. Journal of Geophysical Research: Solid Earth, 101, 17447-17455.

Proussevitch, A.A., and Sahagian, D.L. (1998) Dynamics and energetics of bubble growth in magmas: analytical formulation and numerical modeling. Journal of Geophysical Research: Solid Earth, 103, 18223-18251.

Proussevitch, A.A., Sahagian, D.L., and Anderson, A.T. (1993) Dynamics of diffusive bubble growth in magmas: Isothermal case. Journal of Geophysical Research: Solid Earth, 98, 22283-22307.

Preuss, O., Nowak, M., and Ulmer, S. (2014) Simulation of magma ascent prior to the high-risk caldera forming eruptions of Campi Flegrei using continuous decompression experiments and different starting materials. IODP – ICDP Colloquium 2014, Erlangen, Abstract, 115.

Sahagian, D.L., and Proussevitch, A.A. (1998) 3D particle size distributions from 2D observations: stereology for natural applications. Journal of Volcanology and Geothermal Research, 84, 173-196.

Scandone, R., Cashman, K.V., and Malone, S.D. (2007) Magma supply, magma ascent and the style of volcanic eruptions. Earth and Planetary Science Letters, 253, 513-529.

Schiavi. F., Walte, N., Konschak, A. and Keppler, H. (2010) A moissanite cell apparatus for optical in situ observation of crystallizing melts at high-temperature. American Mineralogist, 95, 1069-1079.

Self, S., Zhao, Jing-Xia, Holasek, R.E., Torres, R.C., and King, A.J. (1996) The atmospheric impact of the 1991 Mount Pinatubo eruption. In: Newhall, C.G., Punongbayan, R.S. (eds.), Fire and mud: Eruptions and lahars of Mt. Pinatubo, Philippines, 1098-1115.

Shea, T., Houghton, B.F., Gurioli, L., Cashman, K.V., Hammer, J.E. and Hobden, B.J. (2010) Textural studies of vesicles in volcanic rocks: An integrated methodology. Journal of Volcanology and Geothermal Research, 190, 271-289.

Shimizu, H., Umakoshi, K., Matsuwo, N., Matsushima, T., and Ohta, K. (1997) Seismic activity associated with the magma ascent and dome growth of Unzen Volcano. Unzen International Workshop: Decade Volcano and Scientific Drilling, Proceedings, pp. 42-44.

Shinohara, H. (2008) Excess degassing from volcanoes and its role on eruptive and intrusive activity. Reviews in Geophysics, 46, RG4005, 1-31.

Shishkina, T.A., Botcharnikov, R.E., Holtz, F., Almeev, R.R., and Portnyagin, M.V. (2010) Solubility of H_2O- and CO_2-bearing fluids in tholeiitic basalts at pressures up to 500 MPa. Chemical Geology, 277, 115-125.

Sigurdsson, H. (1982) Volcanic pollution and climate--the 1783 Laki eruption. American Geophysical Union, EOS Transactions, v. 10 August 1982, 601-602.

Sparks, R.S.J. (1978) The dynamics of bubble formation and growth in magmas: a review and analysis. Journal of Volcanology and Geothermal Research, 3, 1-37.

Sparks, R.S.J., and Brazier, S. (1982) New evidence for degassing processes during explosive eruptions. Nature, 295, 218-220.

Sparks, R.S.J., Barclay, J., Jaupart, C., Mader, H.M., and Phillips, J.C. (1994) Physical Aspects of Magma Degassing – I. Experimental and theoretical constraints on vesiculation. In M.R. Carroll and J.R. Holloway, Eds., Volatiles in Magmas, 30, p. 413–445. Reviews in Mineralogy, Chantilly, Virginia.

Sparks, R.S.J., Young, S.R., Barclay, J., Calder, E.S., Cole, P., Darroux, B., Davies, M.A., Druitt, T.H., Harford, C., Herd, R., James, M., Lejeune, A.M., Loughlin, S., Norton, G.,

Skerrit, G., Stasiuk, M.V., Stevens, N.S., Toothill, J., Wadge, G., and Watts, R. (1998) Magma production and growth of the lava dome of the Soufriere Hills Volcano, Montserrat, West Indies: November 1995 to December 1997. Geophysical Research Letters, 25, 3421-3424.

Taylor, J.R., Wall, V.J., and Pownceby, M.I. (1992) The calibration and application of accurate redox sensors. American Mineralogist 77, 284-295.

Toramaru, A. (1989) Vesiculation process and bubble size distributions in ascending magmas with constant velocities. Journal of Geophysical Research, 94, 17523-17542.

Toramaru, A. (1995) Numerical study of nucleation and growth of bubbles in viscous magmas. Journal of Geophysical Research, 100, 1913-1931.

Toramaru, A. (2006) BND (bubble number density) decompression rate meter for explosive volcanic eruptions. Journal of Volcanology and Geothermal Research, 154, 303-316.

Toramaru, A. (2014) On the second nucleation of bubbles in magmas under sudden decompression. Earth and Planetary Science Letters, 404, 190-199.

Tuttle, O.F. (1949) Two pressure vessels for silicate-water studies. Bulletin of Geological Society of America, 60, 1727-1729.

Ulmer, G.C. and Barnes, H.L. (1987) Hydrothermal experimental techniques. New York: John Wiley & Sons.

Walker, D. and Mullins Jr., A.T. (1981) Surface tension of natural silicate melts from 1200°-1500°C and implications for melt structure. Contributions to Mineralogy and Petrology, 76, 455-462.

Williams, D. W. (1966). Externally heated cold seal pressure vessels for use to 1200°C at 1000 bars. Mineralogical Magazine, 35, 1003-1012.

Zajacz, Z., Candela, P.A., Piccoli, P.M., and Sanchez-Valle, C. (2012) The partitioning of sulfur and chlorine between andesite melts and magmatic volatiles and the exchange coefficients of major cations. Geochimica et Cosmochimica Acta, 89, 81-101.

Zajacz, Z., Candela, P.A., Piccoli, P.M., Sanchez-Valle, C. and Wälle, M. (2013) Solubility and partitioning behavior of Au, Cu, Ag and reduced S in magmas. Geochimica et Cosmochimica Acta 112, 288-304.

Zhang, Y., and Ni, H. (2010) Diffusion of H, C, and O Components in Silicate Melts. Reviews in Mineralogy and Geochemistry, 72, 171–225.

Zimova, M., and Webb, S. (2006) The effect of chlorine on the viscosity of Na_2O-Fe_2O_3-Al_2O_3-SiO_2 melts. American Mineralogist, 91, 344-352.

Zimova, M., and Webb, S.L. (2007) The combined effects of chlorine and fluorine on the viscosity of aluminosilicate melts. Geochimica et Cosmochimica Acta, 71, 1553-1562.

Zisman, W.A. (1964). Relation of the equilibrium contact angle to liquid and solid constitution. In R.F. Gould, Ed., Contact Angle, Wettability, and Adhesion, 43, p. 1-51. Advances in Chemistry, American Chemical Society, Washington, DC.

Figure captions

Figure 1. Schematic plot of the 3 major decompression methods: single-step (blue dashed line), multi-step (red solid line) and continuous (black dashed line). The decompression rate for single- and multi-step experiments are averaged and given as a "constant" time-integrated value (= r_{int}). In case of the instantaneous, once-only pressure release of the single-step method, the following annealing step is considered equal to the entire decompression run duration (Δt).

Figure 2. Screenshots of 3D-visualization of bubbles from μ-tomographical scan data for Nowak et al. (2011) experimental end products for **a**) single-step, **b**) multi-step and **c**) continuous decompression of water-saturated rhyodacitic melts, using YaDiV software (Friese et al., 2013).

Figure 3. Heterogeneous bubble nucleation: Relationship between wetting angle (Ψ) and supersaturation pressure (ΔP_N), where wetting angle $\Psi = 180° - \theta$ (θ = contact angle; Gualda and Ghiorso, 2007). It has been proven that Fe-(Ti)-oxides trigger heterogeneous nucleation (e.g., Hurwitz and Navon, 1994) but other minerals (especially oxides and possibly sulfides) may have a similar effect. v.: vapor (fluid); σ: melt-vapor surface tension; ΔF: Helmholtz free energy for creating a curved surface; Φ: wetting factor. The figure was modified after Hurwitz and Navon (1994), Mangan et al. (2004b) and Gualda and Ghiorso (2007). *Please note*: Mangan et al. (2004b) used the term *contact angle* in their Fig. 1 for the "outer angle", which is typically defined as wetting angle (e.g., this study; Zisman, 1964; Gualda and Ghiorso; 2007).

Figure 4a-b. Experimental results for homogeneous bubble nucleation based on experimental approaches using (almost) continuous and constant decompression rates (r). Figure **4a)** shows all

1235 available results for homogeneous bubble nucleation based on (almost) continuous
1236 decompression experiments. A trend predicted by the model of Toramaru (2006) for rhyolitic
1237 melts at 800 °C is plotted for comparison (see Section 5.1 for a detailed description of the
1238 model). The haplogranitic melt composition of Martel and Bureau (2001; MB01) is similar to the
1239 rhyolitic compositions used by the other studies. Pichavant et al. (2013) performed additional
1240 basaltic experiments, which are not shown because they are not directly comparable to the
1241 plotted datasets owing to a change (decrease) in decompression rate during decompression.
1242 Linear regressions are plotted for selected experimental datasets (Fiege et al., 2014; Mangan and
1243 Sisson, 2000; Marxer et al., 2015; Mourtada-Bonnefoi and Laporte, 2004), illustrating that the
1244 results of the different studies follow trends with similar slopes. Figure **4b)** is an enlarged view
1245 of Fig. 4a and shows only selected data for rhyolitic systems at 800 °C. The selected rhyolitic
1246 systems were volatile-saturated prior to decompression and contain initially 0 to 800 ppm bulk
1247 CO_2.
1248 *The run products of Pichavant et al. (2013) contain very small amounts of Fe-Ti-oxides;
1249 however, the bubbles in the center of the capsules are interpreted by the authors to be produced
1250 homogeneous bubble nucleation.
1251 *References in Fig. 4:* Pi13: Pichavant et al. (2013); Fi14: Fiege et al. (2014a); Go11: Gondé et al.
1252 (2011); MS00: Mangan and Sisson (2000); MB01; Martel and Bureau (2001); Ha10: Hamada et
1253 al. (2010); MBL04: Mourtada-Bonnefoi and Laporte (2004); MBL02: Mourtada-Bonnefoi and
1254 Laporte (2002); MBL99: Mourtada-Bonnefoi and Laporte (1999); To06: Toramaru (2006).
1255
1256 **Figure 5a-b.** Experimental results for heterogeneous bubble nucleation based on **a)** single- and
1257 multi-step experiments or **b)** on experimental approaches using (almost) continuous and constant

decompression rates (r). The dashed and dotted lines are just to guide the eyes. Two dotted lines are shown for the dataset of Mangan et al. (2004b) since these results scatter significantly.

*According to unpublished image analysis results of S.B. Cichy, the Fe-(Ti-) oxide content was less than 0.1 vol% in the experiments of Cichy et al. (2011), while the total crystal fraction is rather high (1 to 9 vol%; see Cichy et al, 2011).

Figure 6a-b. Influence of annealing time on BND. The experiments were performed by Fiege et al. (2014; Fi14) using a hydrous (~6.5 wt% H_2O) andesitic melt as starting material (temperature: 1030 °C; pressure was released continuously from 400 to 70 MPa). **a**) log(BND · mm^3) vs. annealing time after fast decompression at a constant rate of 0.1 MPa/s (Fig. 6a was modified after Fiege et al., 2014a). **b**) log(BND · mm^3) vs. integrated decompression rate [$r_{int} = (P_i - P_f) / \Delta t$; see Fig. 1]. The intergrated decompression rate was calculated for the experiments shown in Fig. 6a and the results are compared to experiments, which were directly quenched after decompression at different rates (0.0005 to 0.1 MPa/s).

Initial S and Cl contents of the andesitic melt:

a) Experiments GYClA: ~1000 ppm S, ~1000 ppm Cl

b) Exp. GYMClA: ~1000 ppm S; ~500 ppm Cl

c) Exp. QFMA: ~140 ppm S, Cl-free; and QFMClA: ~240 ppm S, 1000 ppm Cl

d) Exp.: GYClA and GYMClA, see a) and b) for contents

Figure 7a-b. Correlation between bubble number density BND, decompression rate r and melt viscosity η for water-undersaturated melts prior to decompression. Only experiments with short run durations of Gondé et al. (2011) were considered to minimize the possible influence of water

loss during their experiments (see Section 5.1 for details). The presented melt viscosities [Pa·s] are average values (error: 2 sigma of mean) calculated based on the two values predicted by the viscosity model of Hui and Zhang (2007) and of Giordano et al. (2008), respectively. **a**) log(BND · mm^3) vs. decompression rate [MPa/s]. The trends were predicted using equation 6 and 7 (Section 5.1). **b**) Y-axis intercept vs. melt viscosity. Only average values for each melt composition and temperature are shown. The equations for the two regressions are given in the text. The black trend is based on all results shown in Fig. 7b), while the experiments of Pichavant et al. (2013) and Fiege et al. (2014a) are excluded for the calculation of the dashed blue trend (see Section 5.1 for details).

References in Fig. 7: Pi13: Pichavant et al. (2013); Fi14: Fiege et al. (2014a); Go11: Gondé et al. (2011); MB01; Martel and Bureau (2001).

*Y-axis intercept of the trends in Fig. 7a on a log(BND · mm^3) vs. log(r · s/MPa] plot, assuming a slop of 1.5 (see Section 5.1 for details).

Table 1: Compilation of experimental studies and relevant conditions on decompression-induced bubble formation in silicate melts using (almost) continuous decompression rates and selected studies using single-step technique. Only conditions of experiments which produced bubbles and for which BND was determined are listed.

Melt composition	*$P_{initial}$ [MPa]*	*P_{final} [MPa]*	*T [°C]*	*Annealing time t_A [h or s]*	*Decompression rates [MPa/s]*	*Volatiles*	*H_2O-saturated or -undersaturated*	*Continuous, multi-, or single-step*	*Experimental device*	*Reference*
homogenous bubble nucleation										
rhyolite	285	172	800	120 s	0.77	H_2O	saturated	(quasi) continuous	CSPV	Mourtada-Bonnefoi and Laport (1999)
rhyolite	200	25 to 50	900	--	0.025 to 8.5	H_2O (traces of CO_2)	saturated	continuous	CSPV	Mangan and Sisson (2000)
haplogranite (rhyolite)	960 to 1220	~580 to 1245 #	~740 to 850 #	--	2.3 to 49.0	H_2O	saturated	continuous #	DA	Martel and Bureau (2001)
rhyolite	200 to 295	29 to 246	800	1 to 122 s (one at 1.5 h)	0.30 to 6.32	H_2O±CO_2	saturated	(quasi) continuous	CSPV	Mourtada-Bonnefoi and Laport (2002)
rhyolite	260	58.9 to 88.6	800	--	0.0278 to 1.24	H_2O	saturated	multi-step (almost continuous)*	CSPV	Mourtada-Bonnefoi and Laport (2004)
rhyolite	250	30 to 75	700 to 800	--	0.7 to 90	H_2O	saturated	continuous	IHPV	Hamada et al. (2010)
haplogranite (rhyolite)	288 to 363	4 to 205	900 to 1000	--	0.06 to 0.75	H_2O	undersaturated	continuous	TIHPV	Gondé et al. (2011)
phonolite	200	75 to 150	1050	--	0.0028 to 1.7	H_2O	mainly saturated	continuous, multi- and single-step	IHPV	Marxer et al. (2015)
basalt	195 to 200	45 to 48	1150	--	0.017 to 0.027	H_2O+CO_2	undersaturated	continuous	IHPV	Pichavant et. al. (2013) ¶
(dac.) andesite	400	70	1030	0 to 72 h	0.0005 to 0.1	H_2O+S±Cl	undersaturated	continuous	IHPV	Fiege et al. (2014)
(dac.) andesite	400	70 to 150	1030	--	0.1	H_2O (+S)	undersaturated	continuous	IHPV	*this study*
heterogeneous bubble nucleation										
rhyolite	200	50 to 175	900	--	0.003 to 8.5	H_2O (traces of CO_2)	saturated	continuous	CSPV	Mangan and Sission (2000)
rhyolite	200	100 to 175	850	--	0.003 to 4.2	H_2O+CO_2	saturated	continuous	CSPV	Mangan et al. (2004a)
dacite	200	50 to 170	950	--	0.60 to 1.64	H_2O	saturated	continuous	CSPV	Mangan et al. (2004b)
rhyolite	200	20.5 to 67.7	800	--	0.0278 to 1.01	H_2O+CO_2	saturated	continuous	CSPV	Cluzel et al. (2008)
rhyodacite	300	50	850	--	0.0002 to 20	H_2O±CO_2	saturated	continuous, multi- and single-step	CSPV	Cichy et al. (2011)
rhyolite	50 to 175	30 to 145	740 to 800	15 s to 6 h	0.0012 to 7.0	H_2O	saturated	single-step	CSPV	Gardner and Denis (2004)
rhyolite	50 to 125	17.5 to 90	550 to 700	30 to 180 s	0.11 to 2.42	H_2O	saturated	single-step	CSPV	Gardner (2007)

*Step size was <1 MPa leading to an almost continuous decompression. CSPV: Cold sealed pressure vessel or externally heated pressure vessel; IHPV: Internally heated pressure vessel; TIHPV: Transparent internally heated pressure vessel using sapphire windows; DA: Bassett-type hydrothermal diamond-anvil cell. # Decompression is induced by cooling. ¶ The run products contain very small amounts of Fe-Ti-oxides; however, the bubbles in the center of the capsules are interpreted to be produced homogeneous bubble nucleation.

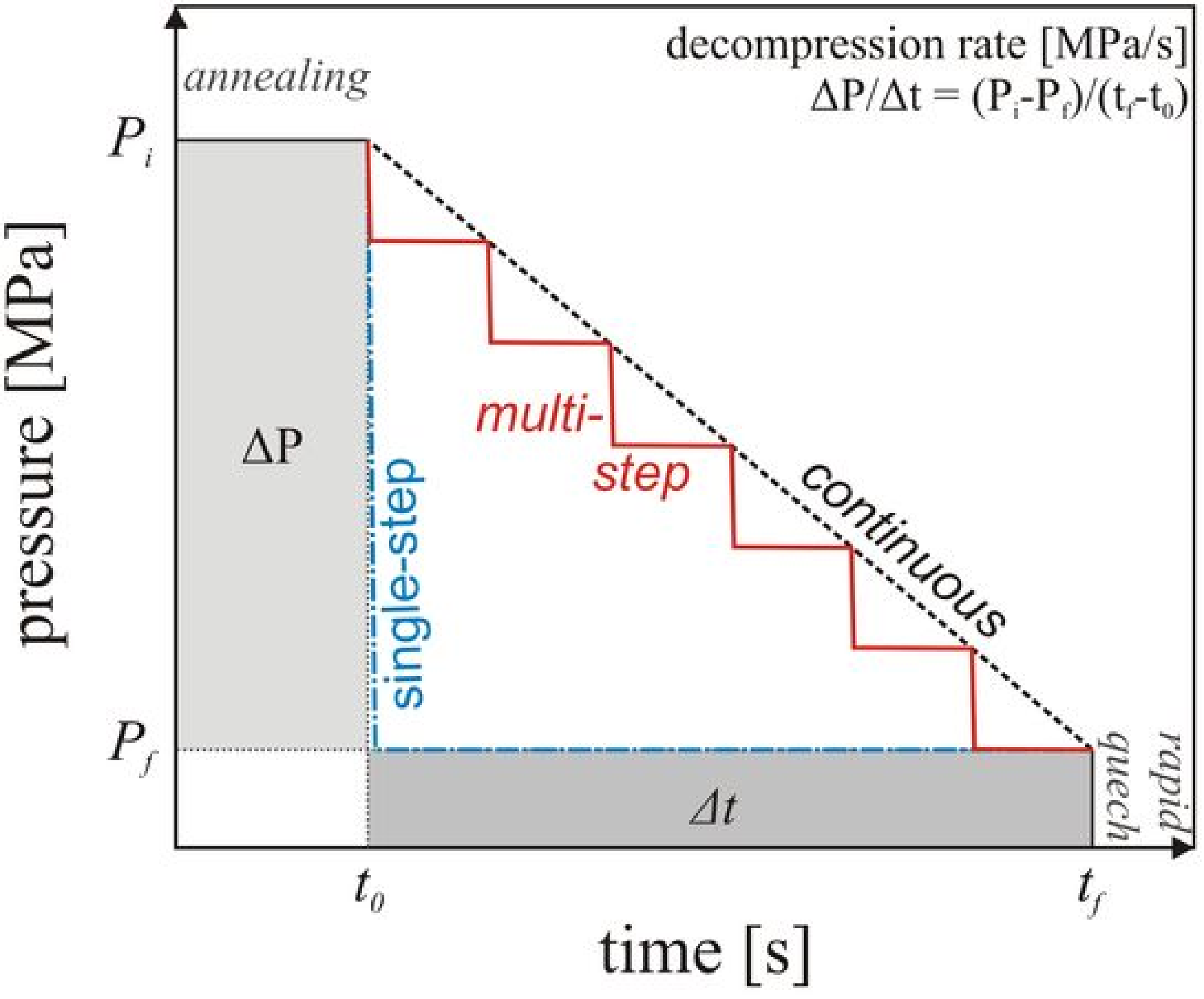
decompression rate [MPa/s]
$\Delta P/\Delta t = (P_i - P_f)/(t_f - t_0)$
annealing
P_i
P_f
ΔP
single-step
multi-
step
continuous
rapid
quench
Δt
t_0
t_f
pressure [MPa]
time [s]

a) single-step

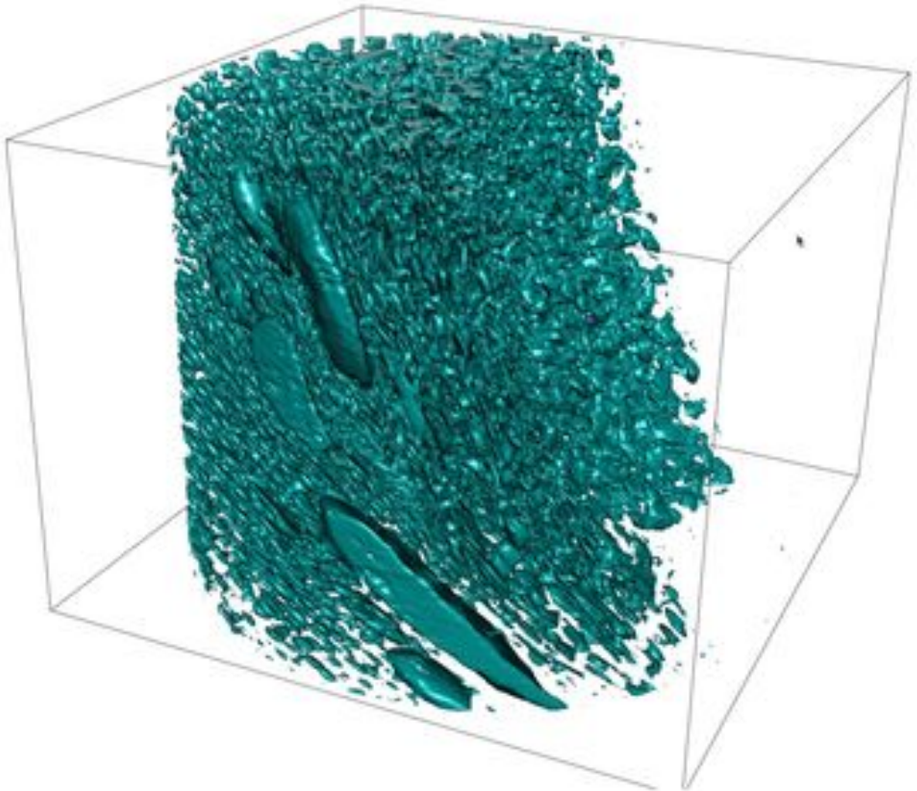

b) multi-step

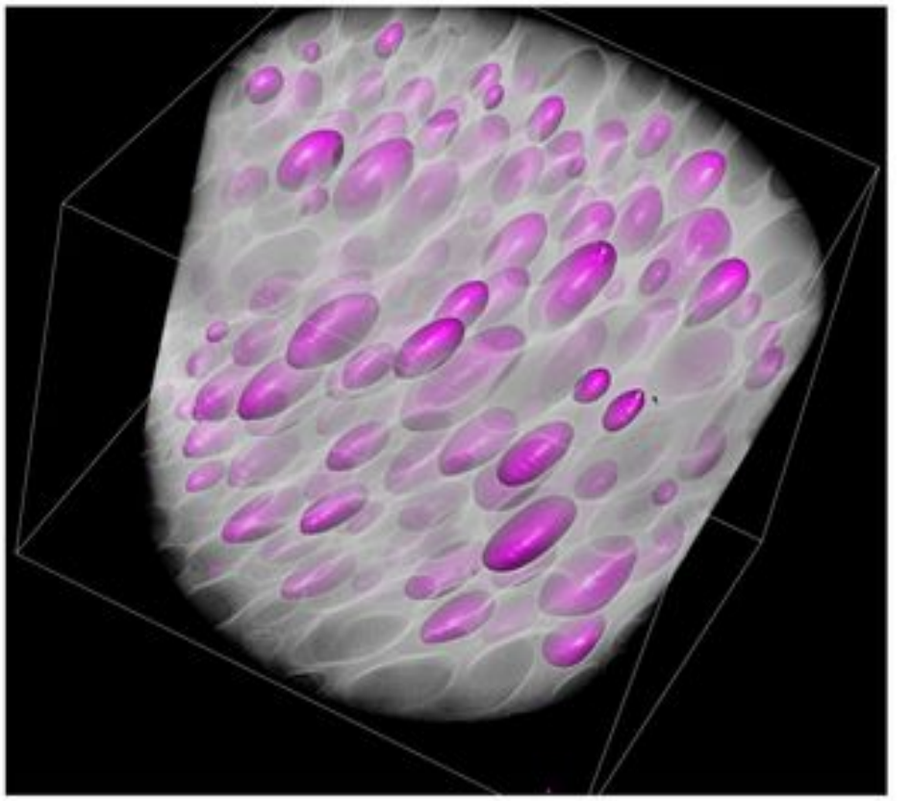

c) contiuous

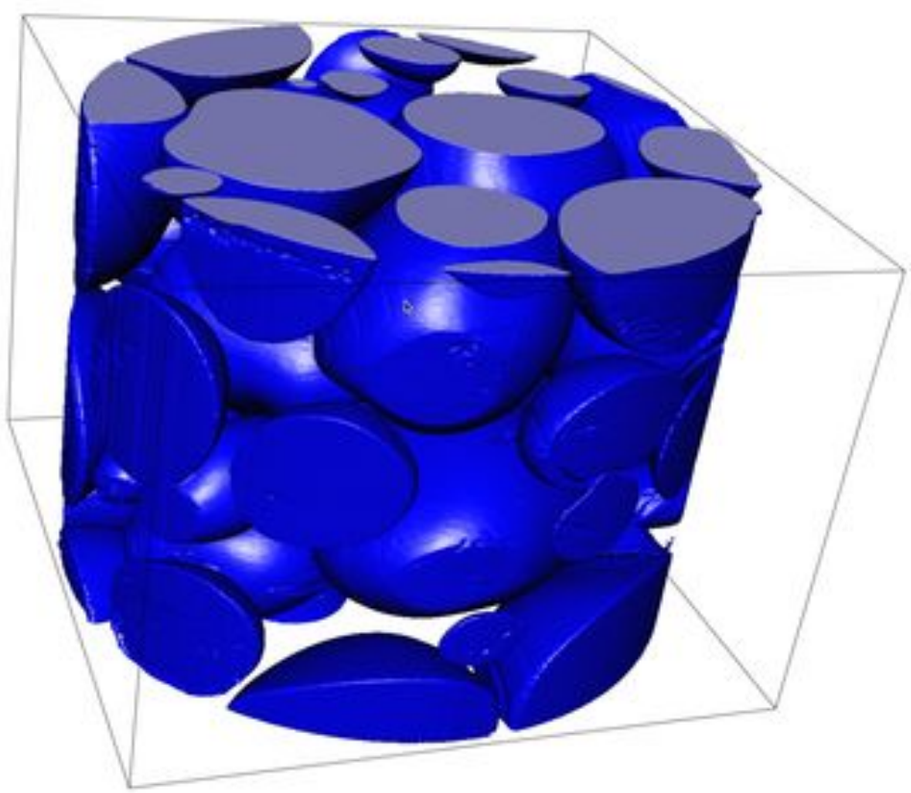

box sizes (x, y, z):
0.76mm, 0.76mm, 0.76mm
rock sample volumes:
0.35mm³ (cylindrical)

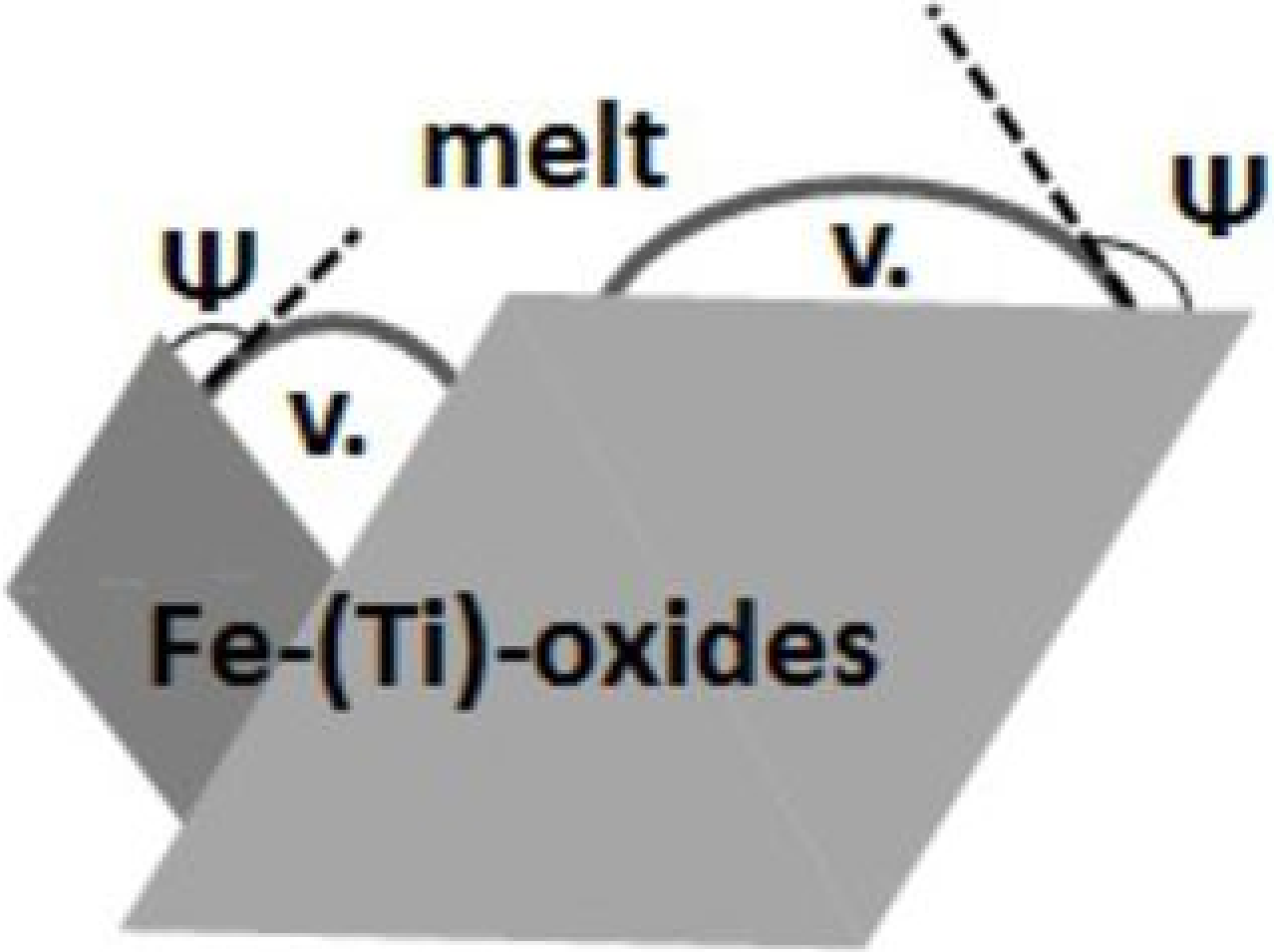

$$\Delta P_N = \sqrt{\frac{16 \cdot \pi \cdot \sigma^3 \cdot \Phi}{3 \cdot \Delta F}}$$

$$\Phi = (2 - \cos(\Psi)) \cdot (1 + \cos(\Psi))^2 / 4$$

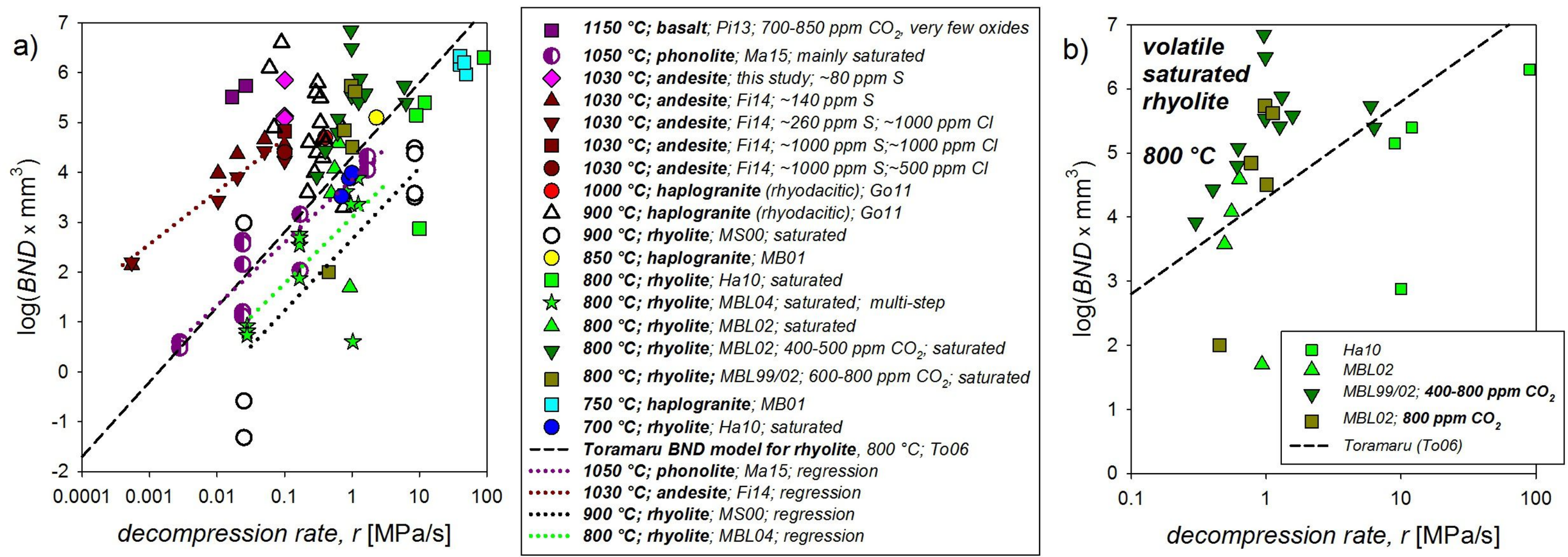
a)
log(BND x mm3)
decompression rate, r [MPa/s]
0.0001
0.001
0.01
0.1
1
10
100
-2
-1
0
1
2
3
4
5
6
7
1150 °C; basalt; Pi13; 700-850 ppm CO2, very few oxides
1050 °C; phonolite; Ma15; mainly saturated
1030 °C; andesite; this study; ~80 ppm S
1030 °C; andesite; Fi14; ~140 ppm S
1030 °C; andesite; Fi14; ~260 ppm S; ~1000 ppm Cl
1030 °C; andesite; Fi14; ~1000 ppm S;~1000 ppm Cl
1030 °C; andesite; Fi14; ~1000 ppm S;~500 ppm Cl
1000 °C; haplogranite (rhyodacitic); Go11
900 °C; haplogranite (rhyodacitic); Go11
900 °C; rhyolite; MS00; saturated
850 °C; haplogranite; MB01
800 °C; rhyolite; Ha10; saturated
800 °C; rhyolite; MBL04; saturated; multi-step
800 °C; rhyolite; MBL02; saturated
800 °C; rhyolite; MBL02; 400-500 ppm CO2; saturated
800 °C; rhyolite; MBL99/02; 600-800 ppm CO2; saturated
750 °C; haplogranite; MB01
700 °C; rhyolite; Ha10; saturated
Toramaru BND model for rhyolite, 800 °C; To06
1050 °C; phonolite; Ma15; regression
1030 °C; andesite; Fi14; regression
900 °C; rhyolite; MS00; regression
800 °C; rhyolite; MBL04; regression
b)
volatile saturated rhyolite
800 °C
log(BND x mm3)
decompression rate, r [MPa/s]
0.1
1
10
100
0
1
2
3
4
5
6
7
Ha10
MBL02
MBL99/02; 400-800 ppm CO2
MBL02; 800 ppm CO2
Toramaru (To06)

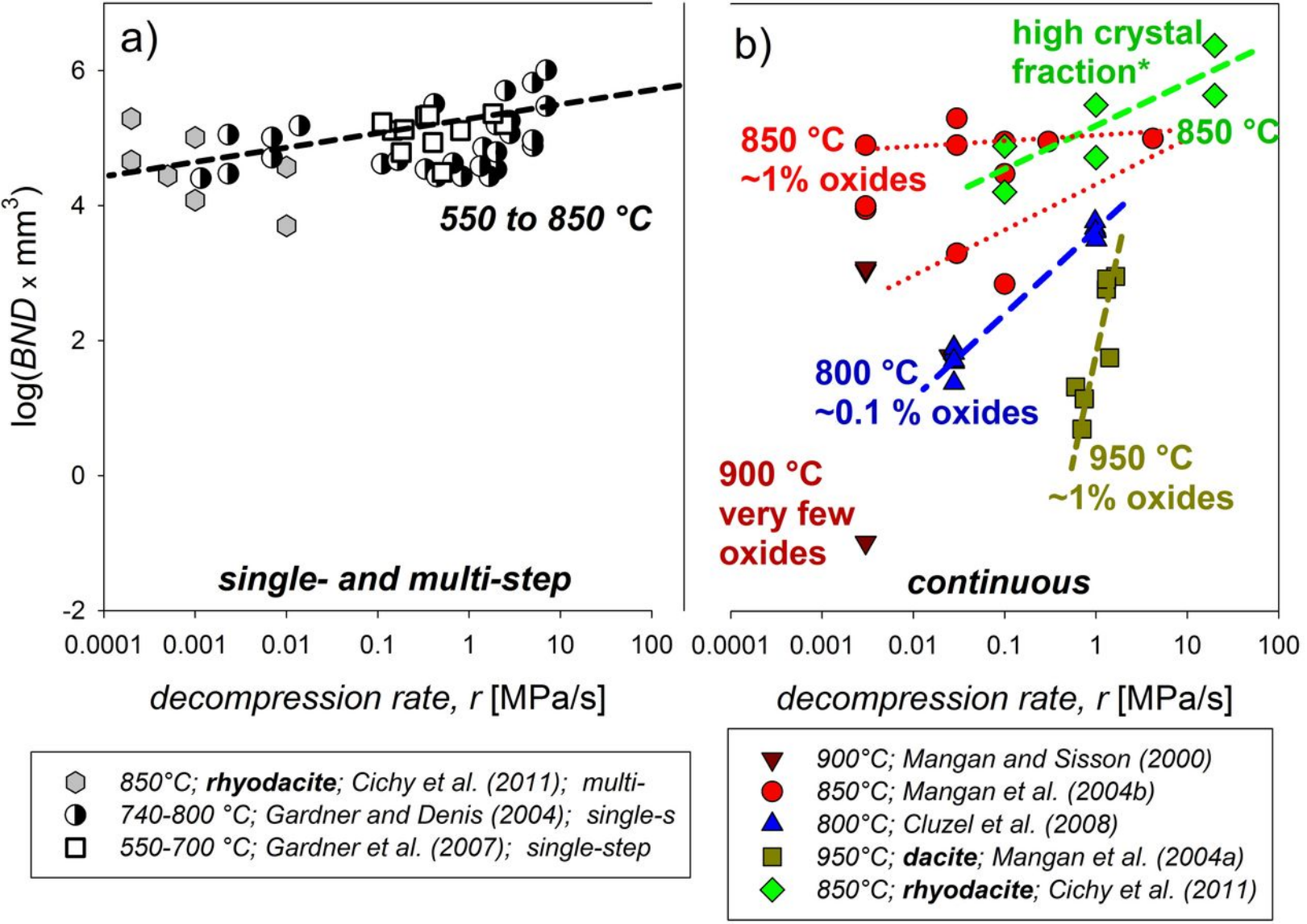
a)
b)
log(BND x mm3)
6
4
2
0
-2
0.0001
0.001
0.01
0.1
1
10
100
550 to 850 °C
single- and multi-step
high crystal fraction*
850 °C
~1% oxides
850 °C
800 °C
~0.1 % oxides
950 °C
~1% oxides
900 °C
very few oxides
continuous
decompression rate, r [MPa/s]
decompression rate, r [MPa/s]
850°C; rhyodacite; Cichy et al. (2011); multi-
740-800 °C; Gardner and Denis (2004); single-s
550-700 °C; Gardner et al. (2007); single-step
900°C; Mangan and Sisson (2000)
850°C; Mangan et al. (2004b)
800°C; Cluzel et al. (2008)
950°C; dacite; Mangan et al. (2004a)
850°C; rhyodacite; Cichy et al. (2011)

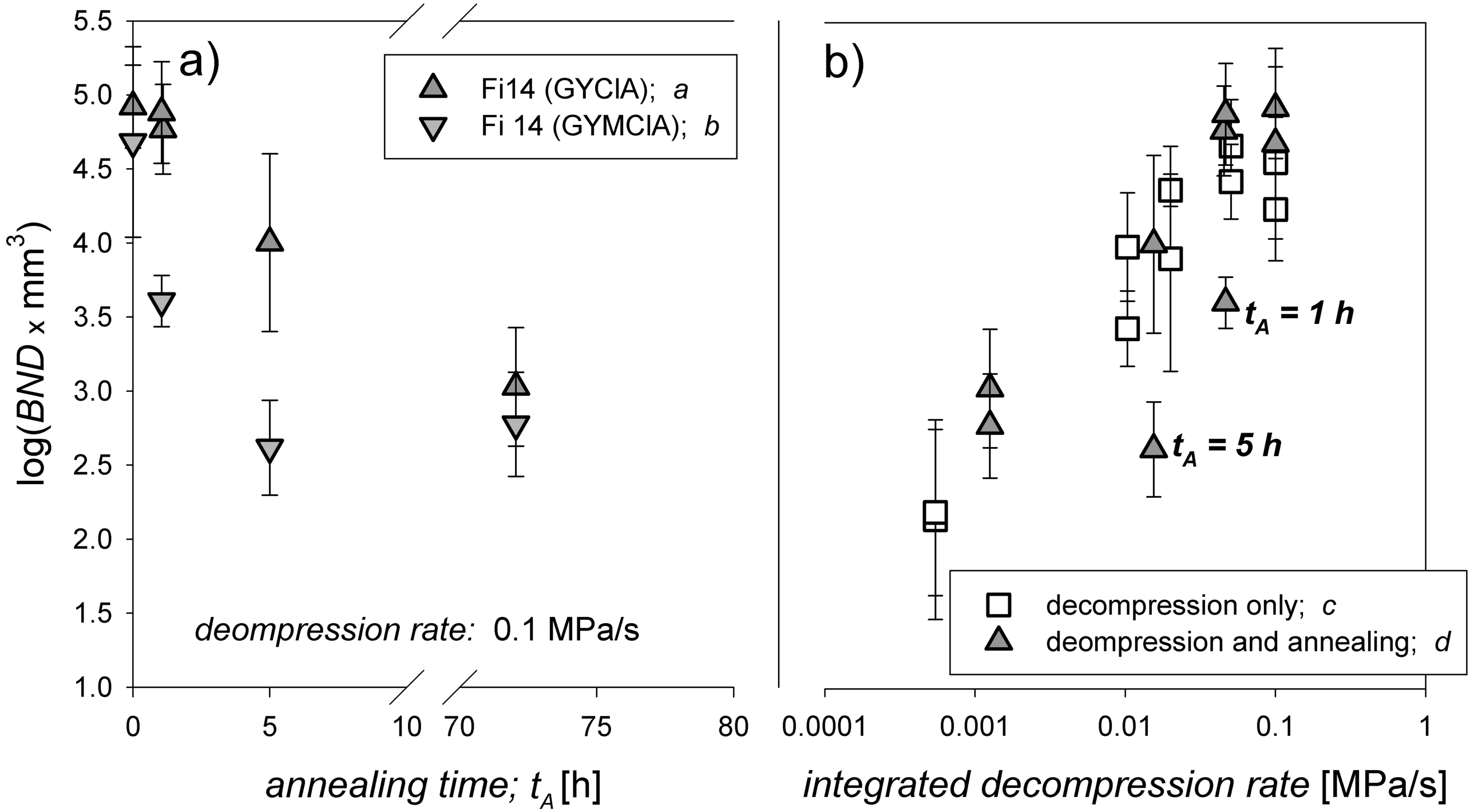
a)
b)
Fi14 (GYClA); a
Fi 14 (GYMClA); b
deompression rate: 0.1 MPa/s
log(BND x mm3)
annealing time; tA [h]
integrated decompression rate [MPa/s]
tA = 1 h
tA = 5 h
decompression only; c
deompression and annealing; d
5.5
5.0
4.5
4.0
3.5
3.0
2.5
2.0
1.5
1.0
0
5
10
70
75
80
0.0001
0.001
0.01
0.1
1

a)

log(*BND* x mm^3)

6
4
2
0
-2

0.0001 0.001 0.01 0.1 1 10 100

decompression rate; *r* [MPa/s]

Y-axis intercept on a log(r) plot

b)

Y-axis intersect [on a log(r) plot]*

12
10
8
6
4
2

0 2 4 6 8 10

melt viscosity; log (η [Pa s])

equation (8)

equation (7)

basalt; 1150 °C; log[η/(Pa s)] ~ 0.79; *Pi13*
andesite; 1030 °C; log[η/(Pa s)] ~ 2.27; *this study*
andesite; 1030 °C; log[η/(Pa s)] ~ 2.24; *Fi14*
HPG; 1000 °C; log[η/(Pa s)] ~ 2.97; *Go11*
HPG; 900 °C; log[η/(Pa s)] ~ 3.59; *Go11*
HPG; 850 °C; log[(η/(Pa s)] ~ 6.31; *MB01*
HPG; 750 °C; log[η/(Pa s)] ~ 6.99; *MB01*

log[η/(Pa s)] ~ 0.79
log[η/(Pa s)] ~ 2.24
log[η/(Pa s)] ~ 2.27
log[η/(Pa s)] ~ 2.97
log[η/(Pa s)] ~ 3.59
log[η/(Pa s)] ~ 6.31
log[η/(Pa s)] ~ 6.99

predicted trends

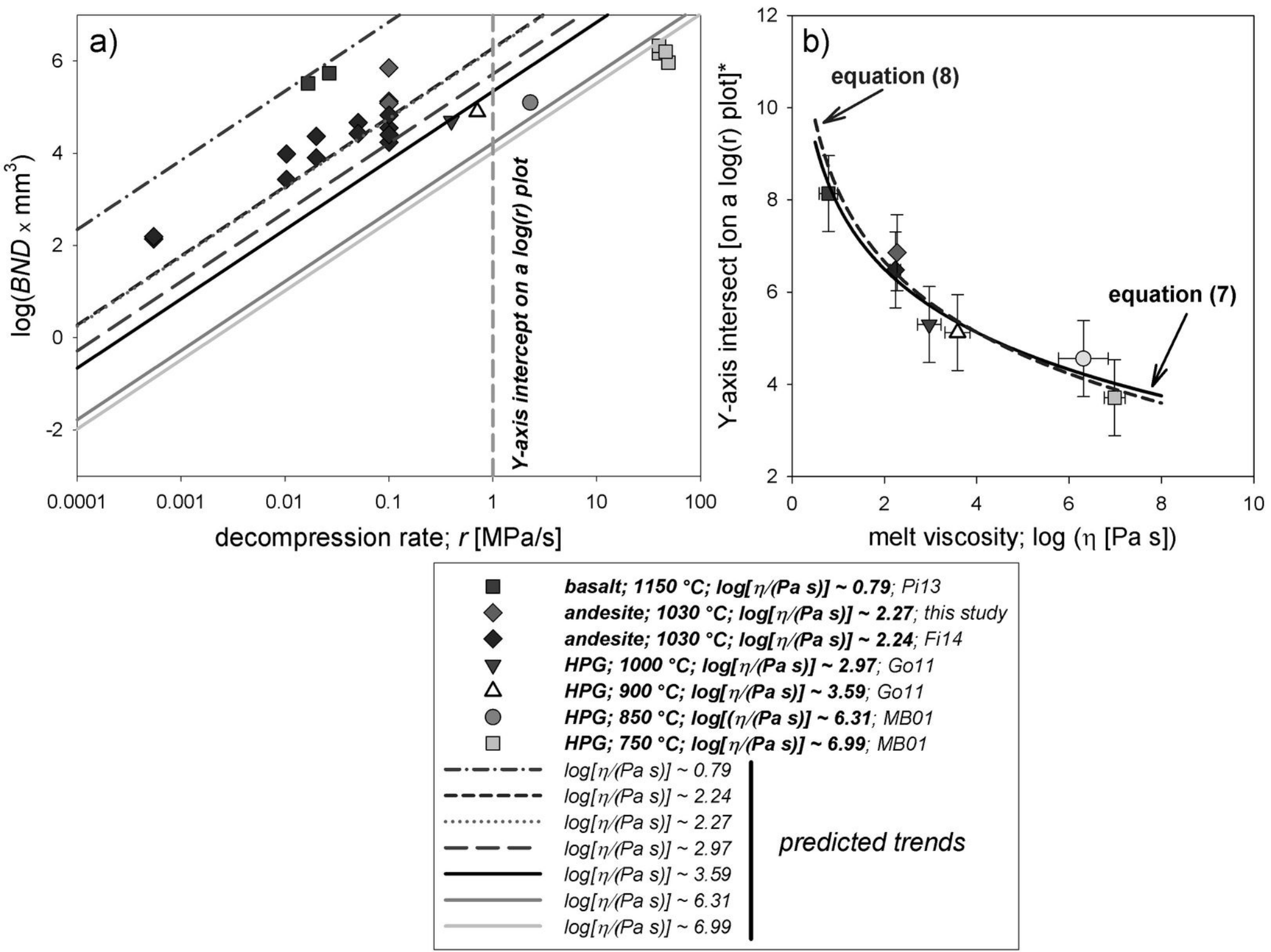
a)
b)
log(BND x mm3)
decompression rate; r [MPa/s]
Y-axis intercept on a log(r) plot
Y-axis intersect [on a log(r) plot]*
melt viscosity; log (η [Pa s])
equation (8)
equation (7)
basalt; 1150 °C; log[η/(Pa s)] ~ 0.79; Pi13
andesite; 1030 °C; log[η/(Pa s)] ~ 2.27; this study
andesite; 1030 °C; log[η/(Pa s)] ~ 2.24; Fi14
HPG; 1000 °C; log[η/(Pa s)] ~ 2.97; Go11
HPG; 900 °C; log[η/(Pa s)] ~ 3.59; Go11
HPG; 850 °C; log[(η/(Pa s)] ~ 6.31; MB01
HPG; 750 °C; log[η/(Pa s)] ~ 6.99; MB01
log[η/(Pa s)] ~ 0.79
log[η/(Pa s)] ~ 2.24
log[η/(Pa s)] ~ 2.27
log[η/(Pa s)] ~ 2.97
log[η/(Pa s)] ~ 3.59
log[η/(Pa s)] ~ 6.31
log[η/(Pa s)] ~ 6.99
predicted trends